

Major and Trace Element and Sr, Nd, Hf, and Pb Isotope Compositions of the Karoo Large Igneous Province, Botswana–Zimbabwe: Lithosphere vs Mantle Plume Contribution

**F. JOURDAN^{1,2,3*}, H. BERTRAND², U. SCHÄRER¹,
J. BLICHERT-TOFT², G. FÉRAUD¹ AND A. B. KAMPUNZU^{4†}**

¹UMR-CNRS 6526 GÉOSCIENCES AZUR, UNIVERSITÉ DE NICE-SOPHIA ANTIPOLIS, 06108 NICE, FRANCE

²UMR-CNRS 5570, ÉCOLE NORMALE SUPÉRIEURE DE LYON ET UNIVERSITÉ CLAUDE BERNARD, 69364 LYON, FRANCE

³BERKELEY GEOCHRONOLOGY CENTER, 2455 RIDGE ROAD, BERKELEY, CA 94709, USA

⁴DEPARTMENT OF GEOLOGY, UNIVERSITY OF BOTSWANA, GABORONE, BOTSWANA

**RECEIVED JULY 18, 2006; ACCEPTED FEBRUARY 22, 2007
ADVANCE ACCESS PUBLICATION APRIL 28, 2007**

We report major and trace element abundances for 147 samples and Sr, Nd, Hf, and Pb isotope compositions for a 36 sample subset of basaltic lava flows, sills, and dykes from the Karoo continental flood basalt (CFB) province in Botswana, Zimbabwe, and northern South Africa. Both low- and high-Ti ($\text{TiO}_2 < 2 \text{ wt } \%$ and $> 2 \text{ wt } \%$) rocks are included. MELTS modeling shows that these magmas evolved at low pressure (1 kbar) through fractional crystallization of gabbroic assemblages. Whereas both groups display enrichment in light rare earth elements (LREE) relative to heavy REE (HREE) and high field strength elements, and systematic negative Nb anomalies, they differ in terms of contrasting middle REE (MREE) to HREE fractionation, which is greater for the high-Ti basalts. This reflects different depths of melting of slightly enriched mantle sources: calculations suggest that the low-Ti basalts were generated by melting of a shallow spinel-bearing (2 % spinel) lherzolite, whereas the high-Ti magmas originated from a deeper-seated garnet-bearing (2–7% garnet) lherzolite. In most isotope plots, the high-Ti lavas together with the picrites define a common trend from Bulk Silicate Earth (BSE) to compositions with strongly negative ϵ_{Nd} and ϵ_{Hf} akin to those of some nephelinites and lamproites. The low-Ti rocks are shifted from BSE-like to more radiogenic Sr isotope ratios, indicative of upper crustal contamination. Trace element and isotope characteristics of the Karoo magmas require a combination of enrichment processes (subduction induced?) and long-term isolation

of the mantle sources. We propose two distinct scenarios to explain the origin of the Karoo province. The first calls for polybaric melting of spatially heterogeneous, partially veined, sub-continental lithospheric mantle (SCLM). Calculations show that mixing between SCLM (\sim BSE) and a strongly Nd–Hf unradiogenic nephelinite-like component (sediment input?) could account for the compositional variations of most of the high-Ti group lavas, whereas the mantle composition responsible for the low-Ti magmas is more likely to be similar to a vein-free, metasomatically enriched SCLM component. The second scenario involves mixing between two end-members represented by the SCLM and its deep-seated alkalic veins and a sub-lithospheric (asthenospheric- or ocean island basalt-like?) mantle plume. In this case, the data are compatible with an increasing mantle plume contribution as the plume rises and expands through the lithosphere. Regardless of which of the two scenarios is invoked, the spatial distribution of the low- and high-Ti magmas matches the relative positioning of the cratons and the Limpopo belt in such a way that strong control of the lithosphere on magma composition and distribution is a mandatory requirement of any petrogenetic model applied to the Karoo CFB.

KEY WORDS: Karoo; large igneous province; flood basalts; dyke swarms; major and trace elements; Sr; Nd; Hf; and Pb isotopes

*Corresponding author. Present address: Berkeley Geochronology Center, 2455 Ridge Road, Berkeley, CA 94709, USA.
E-mail: fjourdan@bgc.org

†Deceased in 2004.

© The Author 2007. Published by Oxford University Press. All rights reserved. For Permissions, please e-mail: journals.permissions@oxfordjournals.org

INTRODUCTION

Continental flood basalts (CFB) are among the most remarkable magmatic events on Earth, consisting of vast outpourings of magma during a relatively brief period of time with potentially dramatic consequences for the biosphere and continental breakup (e.g. Courtillot *et al.*, 1999; Courtillot & Renne, 2003). The origin of CFBs is a matter of intense controversy and over recent decades a large number of models have been advocated. They range from 'active' models, which predict a dominant role for an upwelling deep-seated mantle plume head impinging on the lithosphere (e.g. Campbell & Griffiths, 1990; Hill, 1991), to 'passive' models dominated by plate-boundary forces inducing rifting of heterogeneous lithosphere, and/or thermal incubation beneath mega-continent (Anderson *et al.*, 1992; Anderson, 1994). Combined 'active-passive' models have also been proposed (Courtillot *et al.*, 1999). Contribution from a deep mantle plume source rooted in the core-mantle boundary layer is advocated in the active models, whereas passive models propose upper mantle sources residing in the sub-continental lithospheric mantle (SCLM) and/or the uppermost enriched part of the asthenosphere [the so-called 'perisphere' of Anderson *et al.* (1992)].

The early Jurassic is marked by the emplacement of one of the largest continental flood basalts (CFBs) on Earth ($\geq 3 \times 10^6 \text{ km}^2$). The $\sim 180 \text{ Ma}$ Karoo magmatic province is located in southern Africa, with minor outcrops in Antarctica, and consists of tholeiitic lava flows, sills, and giant radiating dyke swarms emplaced prior to the breakup of southern Gondwana and the opening of the SW Indian Ocean and the Southern Ocean (e.g. Cox, 1988). It was emplaced between 174 and 185 Ma (Fig. 1; Duncan *et al.*, 1997; Jourdan *et al.*, 2005). It consists, at present, of widespread remnants of basalts (lava flows and sills) and giant dyke swarms (Fig. 1).

The so-called 'triple junction' formed by rift structures and pseudo-radiating dyke swarms (Fig. 1) is a key indicator of the widely supported plume origin for the Karoo CFB province (Burke & Dewey, 1972; Campbell & Griffiths, 1990; Ernst & Buchan, 2001). However, the role of a plume head impact on the Karoo triple junction has recently been questioned by the structural inheritance of two and possibly three branches of the triple junction (Watkeys, 2002; Jourdan *et al.*, 2004, 2006), and all geochemical investigations concur that enriched SCLM contributed substantially to the Karoo CFB genesis. Whereas some workers maintain that only the SCLM melted (Duncan *et al.*, 1984; Hawkesworth *et al.*, 1984; Ellam & Cox, 1989; Elburg & Goldberg, 2000), others envisage that the SCLM may have mixed with asthenospheric (plume?) derived magmas (Cox, 1988; Sweeney & Watkeys, 1990; Ellam & Cox, 1991; Sweeney *et al.*, 1991, 1994) with an ocean island basalt (OIB)-like signature (Ellam *et al.*, 1992). Therefore, the various scenarios

currently proposed for the origin of the Karoo CFB (passive or active rifting models) are conflicting and incomplete, as they rest on insufficient geochemical data obtained for only a few localized areas, ignoring crucial regions such as the northwestern part of the Karoo CFB and the northern branches of the giant dyke system.

Here we attempt to bridge this gap by presenting major and trace element and Sr, Nd, Hf, and Pb isotopic data for the extensive lava flows and sills from Botswana and the dykes from the two northern giant dyke swarms; that is, the Okavango and the Save-Limpopo dyke swarms (Fig. 1). This study is the first comprehensive investigation of the northwestern Karoo. In addition to providing an extended database for this area, our work also aims at (1) constraining the origin of the low- and high-Ti magmatism characterizing the Karoo CFB province and (2) tentatively outlining two possible scenarios for the origin of the Karoo CFB.

OVERVIEW OF THE KAROO MAGMATIC PROVINCE

The Karoo province in southern Africa

The Karoo magmatism in southern Africa consists of a vast cover of lava flows and sills, giant dyke swarms, and more localized intrusive centers (Fig. 1), intruding the Archaean Kaapvaal and Zimbabwe cratons, the Paleo-Proterozoic Limpopo belt, and the Permian-Jurassic Karoo sedimentary cover (Eales *et al.*, 1984; Carney *et al.*, 1994; Key & Ayres, 2000).

The main dyke systems are the N110° Okavango dyke swarm, the N70° Save-Limpopo dyke swarm, and the north-souths north Lebombo and Rooi Rand dyke swarms, all of them dominantly basaltic. The Okavango and Save-Limpopo dyke swarms, mainly exposed in Botswana (and partly in Zimbabwe), have been dated recently by the $^{40}\text{Ar}/^{39}\text{Ar}$ method at $\sim 179 \text{ Ma}$ ($n=18$; Le Gall *et al.*, 2002; Jourdan *et al.*, 2004, 2005) and are thus inferred to represent a brief tectono-magmatic event. The Olifants River dyke swarm, previously proposed to be part of the Karoo province (e.g. Ernst & Buchan, 2001), can no longer be considered as a Karoo swarm because of its Proterozoic-Archaean age (Marsh, 2002; Jourdan *et al.*, 2006).

Karoo lava remnants are present over most of southern Africa and include the following.

- (1) The Lesotho basaltic lava pile (Marsh *et al.*, 1997), which has yielded five plagioclase $^{40}\text{Ar}/^{39}\text{Ar}$ ages ranging between 182.3 ± 1.8 and $181.2 \pm 1.6 \text{ Ma}$ (2σ ; Jourdan *et al.*, in press) and one (outlier?) plagioclase age at $183.9 \pm 1.4 \text{ Ma}$ (Duncan *et al.*, 1997).
- (2) The $\sim 10 \text{ km}$ thick Lebombo lava pile, forming a 700 km long monoclinally rifted margin at the eastern edge of the Kaapvaal craton (Watkeys, 2002) and

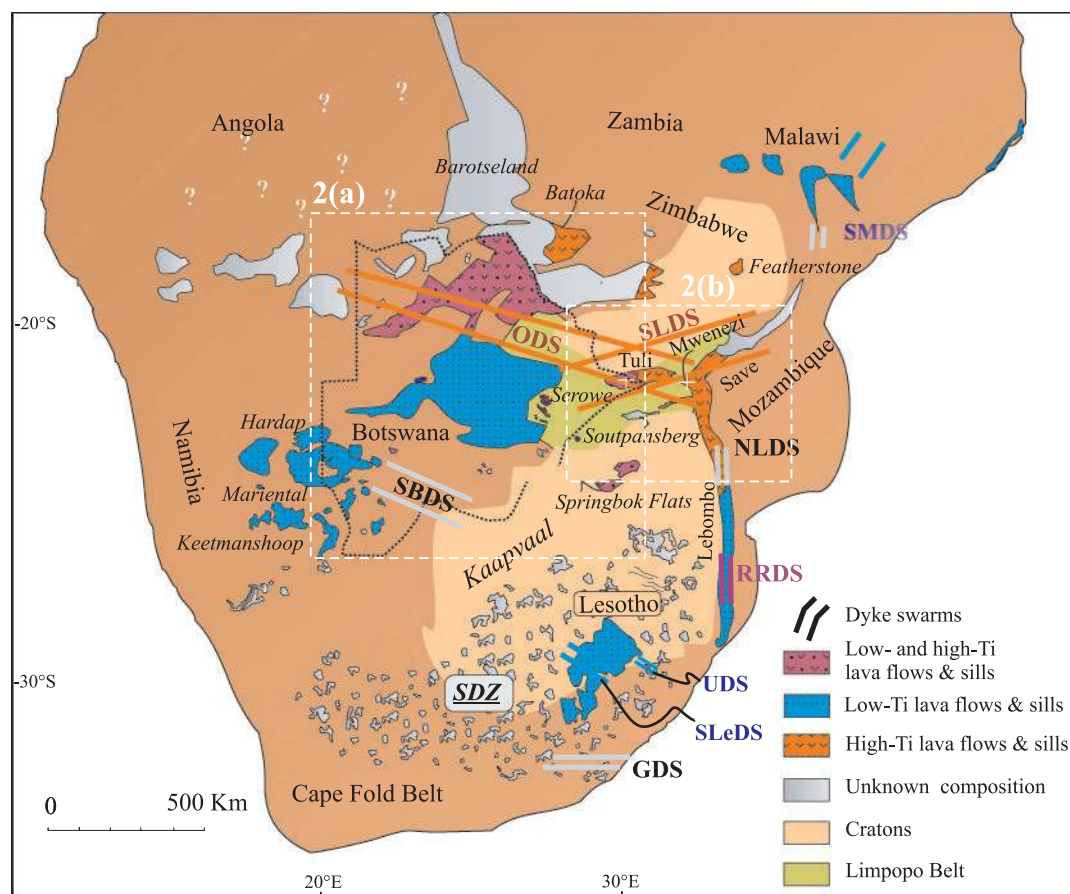


Fig. 1. Sketch map of southern Africa showing the distribution of the Karoo magmatism and related dyke swarms [modified from Jourdan *et al.* (2004) and references therein]. The distributions of low-Ti ($\text{TiO}_2 < 2 \text{ wt } \%$), high-Ti ($\text{TiO}_2 > 2 \text{ wt } \%$), and unknown compositions are indicated (see text for references). The overlap between the low- and high-Ti magmatism in the Tuli basin and northern Botswana should be noted. Dyke swarms are color-coded in orange for high-Ti, blue for low-Ti, and grey for unknown compositions (likewise for lava flows and sills) and are quoted with their abbreviated names: ODS, Okavango dyke swarm; SLDS, Save–Limpopo dyke swarm; SBDS, South Botswana dyke swarm; SLeDS, South Lesotho dyke swarm; UDS, Underberg dyke swarm; SMDS, South Malawi dyke swarm; RRDS, Rooi Rand dyke swarm; NLDS, north Lebombo dyke swarm; GDS, Gap dyke swarm. Dotted line corresponds to the Botswana border. The sill dense zone (SDZ on map) is schematic, as sills occur as quasi-continuous outcrops in the South Africa Karoo sedimentary basin (see, e.g. Marsh *et al.*, 1997). It should be noted that Botswana and western Zimbabwe are covered almost entirely by desert sand and therefore the extents of the Karoo volcanic and intrusive rocks are extrapolated from scarce outcrops, boreholes, and (aero) magnetic data.

- comprising a succession of nephelinitic, picritic, basaltic, and overlying rhyolitic units (e.g. Sweeney *et al.*, 1994, and references therein). The basalts have yielded one $^{40}\text{Ar}/^{39}\text{Ar}$ age of $184.2 \pm 1.2 \text{ Ma}$ on plagioclase separates (Duncan *et al.*, 1997), whereas two north–south dykes cross-cutting the basaltic sequence have provided $^{40}\text{Ar}/^{39}\text{Ar}$ ages of 181.4 ± 0.7 and $182.3 \pm 1.7 \text{ Ma}$ (Jourdan *et al.*, 2005). The rhyolites gave a sensitive high-resolution ion microprobe (SHRIMP) U–Pb age of 180.2 ± 2.7 (Riley *et al.*, 2004) and a plagioclase $^{40}\text{Ar}/^{39}\text{Ar}$ age of $177.8 \pm 0.7 \text{ Ma}$.
- (3) Picrites and basalts capping the Karoo sedimentary sequence in the Mwenzei (= Nuanetsi) basin (Ellam & Cox, 1989, 1991; Ellam *et al.*, 1992).

- (4) Extensive outcrops and subcrops of basaltic lava flows in Botswana (Wigley, 1995) and adjacent Zimbabwe–Zambia (Jones *et al.*, 2001). These formations have been dated recently to be between ~ 177 and 182 Ma by $^{40}\text{Ar}/^{39}\text{Ar}$ on plagioclase separates ($n = 24$; Jones *et al.*, 2001; Jourdan *et al.*, 2005).
- (5) Basaltic lava flows in central Namibia at $183.0 \pm 1.2 \text{ Ma}$ (Duncan *et al.*, 1997).

Vast doleritic sills are particularly striking in South Africa and constitute the main outcrops in the Karoo sedimentary basin. In spite of their widespread distribution, they have so far not been dated, except for one zircon U–Pb age of $183.7 \pm 0.6 \text{ Ma}$ obtained on a granophyric differentiate (Encarnacion *et al.*, 1996). Sills are also

documented in southern and eastern Namibia and (as sub-crops) in western Botswana, and have yielded $^{40}\text{Ar}/^{39}\text{Ar}$ ages on plagioclase separates ranging from 180.5 ± 1.4 to 184.7 ± 1.0 Ma ($n = 3$; Duncan *et al.*, 1997) and 181.0 ± 0.7 to 181.8 ± 1.6 Ma ($n = 2$; Jourdan *et al.*, 2005), respectively. Two dykes from the minor Underberg dyke swarm (Fig. 1), near the Lesotho basalts, have yielded two younger ages at 176.4 ± 1.2 Ma and 176.1 ± 1.2 Ma (Riley *et al.*, 2006). Several gabbroic, syenitic, and granitic intrusive complexes were emplaced in the Mwenezi trough and have yielded $^{40}\text{Ar}/^{39}\text{Ar}$ ages ranging from 178.2 ± 1.7 to 174.4 ± 0.7 Ma ($n = 5$; Jourdan *et al.*, 2007). The north–south-striking Rooi Rand dykes emplaced along the Lebombo monocline show younger ages ranging between 172.1 ± 2.3 and 173.9 ± 0.7 Ma ($n = 3$; Jourdan *et al.*, 2007).

Geochemical studies conducted so far have focused mainly on the lava flows and a few dykes from the eastern and southern parts of the Karoo province, and provide constraints on the origin and genesis of these magmas (see references hereafter). The rocks can be subdivided into five groups.

- (1) The Mashikiri nephelinites (MgO 2.6–12 wt %) are located in the Mwenezi district and display significant incompatible trace element (ITE) enrichment and extremely low ϵNd_i (−9.8 to −20.9) for fairly radiogenic Sr (Harmer *et al.*, 1998). They have been interpreted as reflecting ancient metasomatically enriched SCLM (Hawkesworth *et al.*, 1984; Ellam & Cox, 1991; Harmer *et al.*, 1998).
- (2) The picrites (MgO 10–24 wt %) of the Letaba Formation are mostly restricted to the Mwenezi area, but are of greater volume and extent than the nephelinites. An origin from ancient enriched SCLM akin, but not identical, to the source of the nephelinites was first proposed (e.g. Bristow *et al.* 1984; Hawkesworth *et al.*, 1984; Ellam & Cox, 1989). Later, the picrites were reinterpreted in terms of mixing between either ambient asthenospheric mantle and SCLM (Ellam & Cox, 1991; Sweeney *et al.*, 1991) or, based on Os isotopes, SCLM and a mantle plume (Ellam & Cox, 1992). Most recently, based on new Pb and Hf isotope data, Ellam (2006) proposed a derivation from either a heterogeneous lithospheric mantle source or a more complex mixture of source components.
- (3) The tholeiitic basalts and dolerites, which constitute the overwhelming majority of Karoo rocks, have been classified into two subgroups, the low- and high-Ti groups, on the basis of their TiO_2 , P_2O_5 , and ITE contents, with the limit set at 2.0–2.5 wt % TiO_2 [first recognized by Cox *et al.* (1965)]. The two groups show strong geographic provinciality (Figs 1 and 2). The high-Ti basalts occur in northern Lebombo, in the Mwenezi and Tuli basins (Cox *et al.*, 1967; Duncan *et al.*, 1984), and in northern Botswana along the

Okavango dyke swarm (Elburg & Goldberg, 2000; Jourdan *et al.*, 2004), as well as in the uppermost lava flows capping the low-Ti lava pile (Wigley, 1995). The low-Ti group is located in southern Lebombo (Sweeney *et al.*, 1994), in Lesotho and southern South Africa (Duncan *et al.*, 1984; Marsh *et al.*, 1997; Riley *et al.*, 2005, 2006), in Namibia (Duncan *et al.*, 1984), and in Botswana, except for the Okavango dyke swarm (Wigley, 1995). Beyond the effects of crustal contamination, the origins of the high- and low-Ti sub-provinces have yet to be agreed upon, as they have so far been ascribed to either heterogeneous SCLM (Duncan *et al.*, 1984; Hawkesworth *et al.*, 1984; Sweeney & Watkeys, 1990; Elburg & Goldberg, 2000) or mixing between asthenospheric mantle and SCLM (Sweeney *et al.*, 1994).

- (4) The rhyolites capping the basaltic lava pile in Lebombo and Mwenezi encompass a wide range of isotopic values from mantle-like to extreme crustal signatures (Betton, 1979; Harris & Erlank, 1992).
- (5) The mid-ocean ridge basalt (MORB)-like Rooi Rand dyke swarm (Fig. 1) emplaced along the southern part of the Lebombo monocline is interpreted as the final stage of Karoo magmatism just prior to the onset of ocean-floor spreading (Hawkesworth *et al.*, 1984; Duncan *et al.*, 1990; Watkeys, 2002).

The Karoo province in Antarctica

In Antarctica, the Karoo magmatic rocks consist of dykes and lava flows cropping out in western Dronning Maud Land (DM), from Vestfjellan to H.U. Svedrupfjella. Detailed descriptions have been given by Luttinen & Furnes (2000) and Riley *et al.* (2005) and thus will be only briefly summarized here. Karoo rocks in Antarctica cover or intrude the Archaean Grunehogna craton, the Mesoproterozoic Maud Belt, and Neoproterozoic rocks of the Ritscherlfly supergroup.

The geochronology of the Karoo province in Antarctica consists of seven published $^{40}\text{Ar}/^{39}\text{Ar}$ mineral ages ranging from ~172 to ~183 Ma (Brewer *et al.*, 1996; Duncan *et al.*, 1997; Zhang *et al.*, 2003). We note that these ages have been obtained using different, not necessarily intercalibrated, standards, rendering their comparison not straightforward.

The rocks have been classified into several groups based on their geographical locations and chemical compositions, with the CT (chemical type) groups being from the Vestfjella area (Luttinen & Furnes, 2000) and the DM groups from various areas of Dronning Maud Land (Riley *et al.*, 2005). The principal groups are for the most part (with the exception of DM3) equivalent to existing rocks in southern Africa and are summarized below.

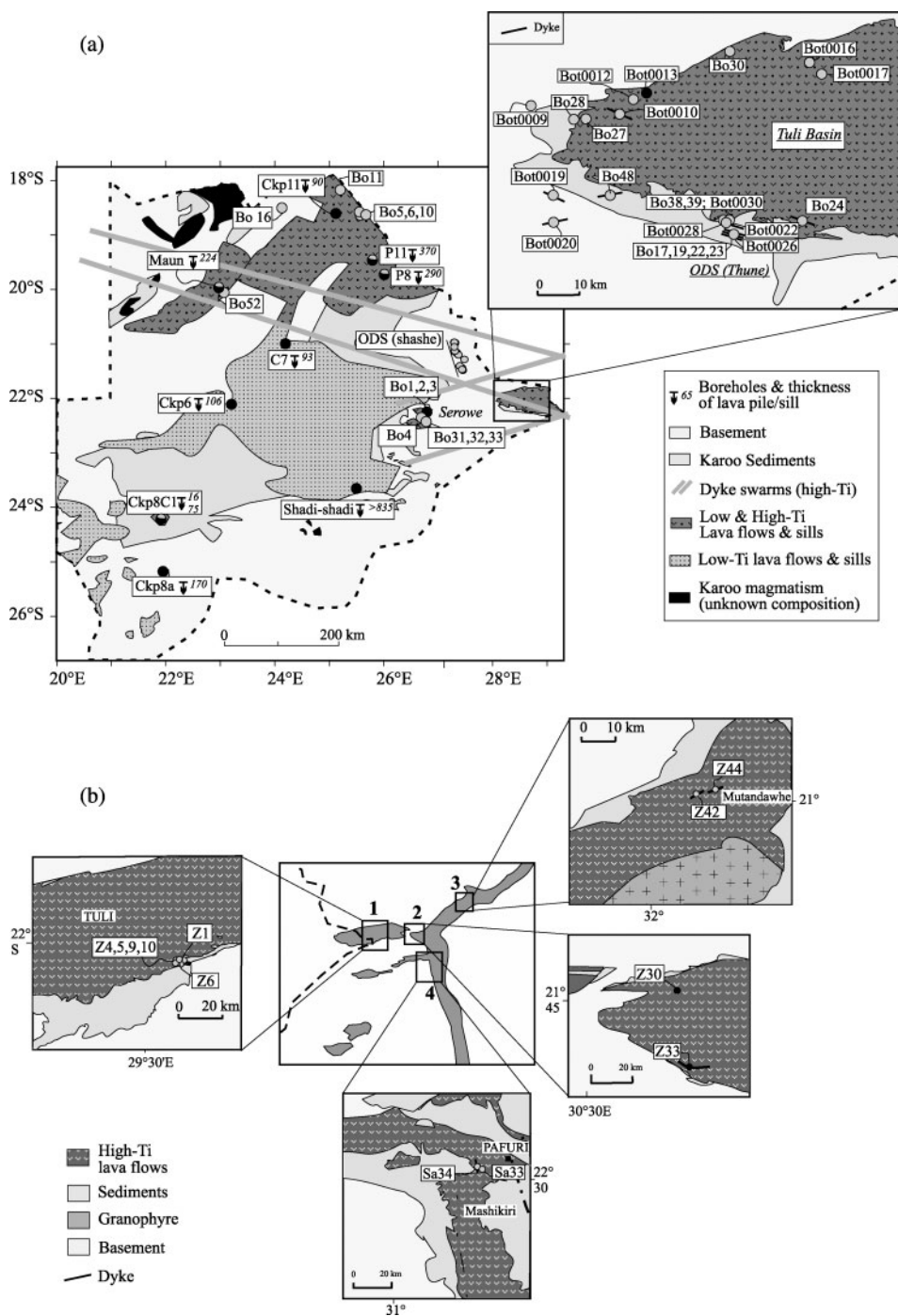


Fig. 2. (a) Sketch map of Botswana showing sample locations and distributions of the low- and high-Ti groups. Boreholes are indicated by downward arrows with the corresponding lava thicknesses (meters) given. Low- and high-Ti rocks collected for this study are indicated by black and grey filled circles, respectively. The direction of the sampled dykes is represented by continuous lines. Inset corresponds to the western part of the Tuli basin. ODS, Okavango dyke swarm. (b) Sketch map of the Karoo triple junction area with the location of the samples in (1) eastern Tuli, (2) Mwenezi (note that the two low-Ti picrites were sampled among high-Ti basalts), (3) Mutandahwe, and (4) north Lebombo.

(1) The CTI and DMI groups have low MgO (<9 wt %) and TiO₂ (<2.2 wt %) contents and moderately enriched Sr isotopic compositions (⁸⁷Sr/⁸⁶Sr ~0.705–0.710) and low εNd_i values (–1 to –15). These groups

have been interpreted as either the products of mixing between a depleted end-member (DM3) and 12% partial melts of the SCLM or a depleted end-member contaminated by the upper crust

- (Riley *et al.*, 2005). They correspond to the low-Ti basalts of southern Africa.
- (2) The CT2 and DM2 groups have variable TiO_2 contents ranging from ~ 2 to ~ 4 wt% and trace element abundances and Sr and Nd isotopic compositions similar to the MORB-like Rooi Rand dyke swarm from southern Africa.
 - (3) The DM3 group is the only group not represented in southern Africa. It consists of basalts, picrites, and ferro-picrites with humpback-shaped rare earth element (REE) and normal MORB (N-MORB)-like incompatible trace element (ITE) patterns. Their isotopic compositions are characterized by remarkably high ϵNd_i (+5 to +9) and unradiogenic $^{87}\text{S}/^{86}\text{Sr}$ (0.7035–0.7062) consistent with derivation from a depleted mantle (plume?) source (Riley *et al.*, 2005).
 - (4) Group 4 includes basaltic and picritic rocks that have high TiO_2 contents (3.8–5.2 wt %) and enriched REE and ITE patterns. These rocks show large variations in Nd and moderate variations in Sr isotopic compositions, and are therefore roughly similar to high-Ti rocks from southern Africa. They have been interpreted as mixing between a MORB source and variable degrees (~ 20 – 30%) of SCLM melts (Riley *et al.*, 2005).

GEOLOGICAL SETTING AND SAMPLING STRATEGY

We focused our sampling efforts on the northern Karoo province, and in particular on the Okavango and Save–Limpopo dyke swarms, as well as on the extensive lava flows and sills of Botswana and southernmost Zimbabwe.

The N110°-trending Okavango dyke swarm extends from northern Namibia to southern Zimbabwe through Botswana (Fig. 2a). Whereas it is hidden by Kalahari sands to the west, it is well exposed to the east, where it intrudes the Zimbabwe Archaean craton, the metamorphic Limpopo–Shashe belt, and the Karoo Permian–Jurassic sedimentary sequence deposited in the Tuli half-graben. The present sample suite, from 77 dykes, was collected primarily along the Shashe river (65 dykes), representing a ~ 100 km long cross-section of the dyke swarm (Le Gall *et al.*, 2002; Jourdan *et al.*, 2004). Additional sampling was carried out in the Tuli half-graben, both in eastern Botswana (Thune river: 10 dykes) and in southern Zimbabwe (one dyke). A further dyke (Bo52), the orientation of which is poorly constrained, was sampled in western Botswana, close to the western extremity of the swarm. The mean width of individual subvertical dykes differs as a function of whether the dykes intrude basement or sedimentary rocks (on average *c.* 18 m and 1.3 m wide, respectively; Le Gall *et al.*, 2005).

The N70°-trending Save–Limpopo dyke swarm is mainly (though poorly) exposed in the SW part of the Tuli basin and surrounding region. It consists of a *c.* 50 km wide swarm including vertical to subvertical dykes with a mean thickness of 27 m (Le Gall *et al.*, 2005). These dykes intrude the metamorphic basement of the Limpopo belt and also crop out in Zimbabwe along and within the Save–Limpopo monocline (Chavez Gomez, 2001). A few dykes with poorly constrained orientations were sampled in northern and eastern Botswana (Bo5, Bo6, Bo4, Fig. 2a).

Lava flows and sills cover most of Botswana and the bordering part of Zimbabwe. Only limited remnants, fortuitously preserved from erosion, are exposed (mainly to the east of the 25°E meridian). Large volumes of basalt are covered by the Kalahari sands over the entire country and are documented by several boreholes (Fig. 2a). The main lava flows are exposed in the Tuli–Mwenezi–North Lebombo area, which is filled in by a ~ 1 km thick volcanic sequence overlying the Karoo sedimentary deposits (Eales *et al.*, 1984; Key & Ayres, 2000). From this sequence, we sampled picritic basalts (nine, four, and two samples from Tuli, Mwenezi, and Lebombo, respectively), the distribution of which is restricted to the lower part of the lava flow. We further collected seven overlying basalts from the Tuli area (Fig. 2a), as well as basalts from several scattered lava flow outcrops in northern Botswana (Bo10, Bo11 and Bo16) and Serowe (Bo1, Bo2, Bo3), where basalts are associated with doleritic plugs (Bo31, Bo32, Bo33) (Fig. 2a).

The sill subcrops, 16–170 m thick, are located in southwestern Botswana and were sampled from boreholes Ckp8Cl, Ckp6 etc. In addition, samples of widespread lava flow subcrops were collected from eight boreholes that recovered a 90 to >835 m thick lava sequence. A 21 lava flow sample suite was collected systematically from a northern borehole (P11 lava flow), whereas only the least altered samples from the other drill cores were selected.

PETROGRAPHY OF THE SAMPLES

The northwestern Karoo doleritic dykes and sills studied here consist of fine- to medium-grained rocks with variable amounts of phenocrysts composed of plagioclase (the most abundant phase), augitic clinopyroxene, occasionally associated with pigeonite, and opaque minerals (titano-magnetite and in some cases ilmenite). Minor olivine phenocrysts occur in some samples. The groundmass comprises a variable mixture of glass and cryptocrystalline plagioclase, pyroxene, Ti-magnetite, and olivine. The N110° and N70° dykes are petrographically indistinguishable. The basaltic lava flows have a similar modal mineralogy

to the dykes, but their textures are more fine-grained with larger amounts of glass and cryptocrystalline mesostasis. Picritic and basaltic picritic dykes and lava flows consist of predominant euhedral olivine phenocrysts (fresh or partially iddingsitized) occurring in a groundmass made of olivine \pm clinopyroxene \pm plagioclase \pm oxides \pm interstitial glass.

Alteration phases are variably developed, depending on the individual sample and are mainly represented by sericite (after plagioclase) and bowlingite or iddingsite (after olivine) along with voids filled by zeolite in the upper part of some of the lava flows.

ANALYTICAL PROCEDURES

A suite of 147 samples were selected for major and trace element analysis. They were crushed and powdered in an agate mill and analyzed by X-ray fluorescence (XRF) using a Philips PW 1404 spectrometer at the University of Lyon. Analytical uncertainties are 1–2% and 10–15%, respectively, for major and trace elements. A total of 133 rocks were also analysed for REE and additional trace elements by inductively coupled plasma mass spectrometry (ICP-MS) at the Chemex Laboratories (Canada), with errors varying from 5 to 10% depending on the concentration of any given element.

Isotope analyses were carried out on 34 rocks and two plagioclase separates selected to be representative of the whole sample suite. Lead and Sr isotope analyses were conducted at the University of Nice. Samples were broken into small chips and carefully separated (in a clean laboratory) to avoid saw marks. Chips were leached with HF and dissolved successively in HF and HCl. Purification and elution of Pb were performed following a modified HBr procedure (Manhès *et al.* 1978; Schärer, 1991). Lead isotopic compositions were measured on an EMI electron multiplier system of a Thomson-206 mass spectrometer, using single zone-refined Re filaments onto which Pb was loaded with H_3PO_4 and silica-gel. Mass fractionation was $0.1 \pm 0.05\%$ a.m.u. for ionization temperatures between 1300 and 1400°C, controlled by the NBS-981 Pb standard, which yielded average ratios of 16.941 ± 0.004 (2σ) for $^{206}\text{Pb}/^{204}\text{Pb}$, 15.501 ± 0.004 for $^{207}\text{Pb}/^{204}\text{Pb}$, and 36.728 ± 0.009 for $^{208}\text{Pb}/^{204}\text{Pb}$ (eight runs). Total procedural Pb blanks were 60–80 pg. Strontium was separated from Rb and purified on Sr-spec resin and deposited on Re filaments with TaF_5 . The Sr isotope measurements were carried out in dynamic double-collector mode using $^{86}\text{Sr}/^{88}\text{Sr} = 0.1194$ for linear mass fractionation correction. Strontium measurement accuracy was controlled using the NBS-987 standard, which yielded a mean value of 0.71026 ± 0.00005 (2σ -STERR) for $^{87}\text{Sr}/^{86}\text{Sr}$. Total procedural Sr blanks ranged between 60 and 100 pg. Both Pb and Sr blanks were negligible compared with the amounts of these elements analyzed.

Hafnium and Nd isotope compositions were determined by multi-collector (MC) ICP-MS using the VG Plasma 54 at the Ecole Normale Supérieure in Lyon (ENSL). Hafnium and Nd chemical separation was carried out at ENSL following the procedures described by Blichert-Toft *et al.* (1997, 2005) and Blichert-Toft (2001). The JMC-475 and La Jolla standards were measured systematically after every two sample analyses to monitor machine performance and gave $^{176}\text{Hf}/^{177}\text{Hf} = 0.282160 \pm 10$ (2σ) and $^{143}\text{Nd}/^{144}\text{Nd} = 0.511858 \pm 18$ (2σ), respectively. Instrumental mass fractionation was corrected relative to $^{179}\text{Hf}/^{177}\text{Hf} = 0.7325$ and $^{146}\text{Nd}/^{144}\text{Nd} = 0.7219$ using an exponential law. Hafnium and Nd total procedural blanks were better than 25 pg. Age corrections of 179 Ma were applied to all four isotope systems using their respective parent isotope decay constants, which in the controversial case of ^{176}Lu was chosen to be the so-called 'terrestrial' decay constant of 1.865×10^{-11} per year (Scherer *et al.*, 2001).

GEOCHEMISTRY

Major elements

The Karoo lavas and dykes from Botswana and western Zimbabwe include a large range of rock types (from picrites to basaltic andesites) and compositions; for example, the Mg-number [atomic ratio of $100\text{Mg}/(\text{Mg} + 0.85\text{Fe}_{\text{tot}})$] ranges from 82 to 31. Following earlier investigators (e.g. Cox *et al.*, 1967; Cox, 1988; Sweeney *et al.*, 1994), the rocks can be subdivided into two major groups on the basis of their TiO_2 and P_2O_5 contents (Table 1 and Electronic Appendix 1, available for downloading at <http://petrology.oxfordjournals.org>): the high-Ti group ($\text{TiO}_2 > 2$ wt %) includes basaltic dykes from the Okavango (78 samples) and Save–Limpopo (four samples) swarms, basaltic lava flows and sills (18 samples), and picrites (13 samples), whereas the low-Ti group ($\text{TiO}_2 < 2$ wt %) comprises only basaltic lava flows (32 samples) and two picrites.

The high-Ti dykes, lava flows, and sills share similar major element compositions characterized in particular by high TiO_2 (2.16–4.42 wt %) and P_2O_5 (0.23–1.00 wt %) contents. They are quartz- to olivine-normative tholeiites and their SiO_2 contents vary from 47.18 to 52.40 wt %, with the exception of one slightly more differentiated (57.08 wt % SiO_2). On the total alkali–silica diagram (TAS; Le Bas *et al.*, 1986; Fig. 3), the dyke rocks define a narrow range of compositions, which lie in the field of basalts straddling the boundary with basaltic andesites (except for Bot0049, which is classified as a trachyandesite). In contrast, the high-Ti lava flows display a slightly wider range of compositions extending up to the field of basaltic trachyandesites. MgO and Mg-number vary from 2.6 to 7.2 wt % and from 31 to 57, respectively, indicating that these samples are moderately to highly evolved. Mg-number

Table 1: Major (wt %) and trace (ppm) element analyses of basaltic and picritic dykes, lavas, and sills from the Karoo province in Botswana and Zimbabwe

Group type:	Okavango dyke swarm (high-Ti)										Picrite (high-Ti)							Picrite (low-Ti)
Location:	Shashe River							Maun	Tuli (B)	Tuli (Z)	Tuli (B)		Tuli (Z)				Nuanetsi (Sabie m.)	
Sample type:	Dyke N110°										Lava flow						Dyke N110°	Lava flow
Depth (m)																		
Sample no.:	Bot0039	Bot0060'	Bot0065	Bot0072	Bot0074	Bot0091	Bot0098	Bo52	Bo19	Z1	Bo38	Bo39	Z4	Z5	Z9	Z10	Z6	Z30
Major elements (wt %)																		
SiO ₂	50.25	49.58	50.06	50.02	49.84	50.95	49.79	49.54	49.64	49.41	48.69	48.10	48.76	49.24	48.85	48.45	47.85	44.46
Al ₂ O ₃	13.98	12.61	13.72	13.41	13.33	13.36	12.26	13.25	13.09	12.67	8.29	8.48	8.18	8.66	8.22	8.53	7.59	7.13
Fe ₂ O ₃	12.77	14.68	12.74	13.75	13.57	13.86	13.77	15.26	14.65	13.83	12.87	12.29	11.84	11.40	11.19	11.65	11.87	14.20
MgO	5.98	5.02	6.22	5.72	5.34	5.31	5.01	4.74	4.92	5.50	15.26	14.11	14.16	13.00	15.21	13.65	16.91	22.48
CaO	10.18	9.51	10.23	10.12	9.48	9.71	9.00	9.11	9.22	9.49	7.43	7.57	7.29	7.48	6.76	7.21	6.26	5.52
Na ₂ O	2.33	2.39	2.39	2.37	2.59	2.52	2.29	2.51	2.38	2.35	1.47	1.58	1.38	1.60	1.42	1.54	1.20	1.26
K ₂ O	0.65	0.90	0.51	0.76	0.59	0.63	1.30	1.02	1.06	0.99	1.15	0.77	2.31	1.85	1.41	2.46	2.02	0.60
TiO ₂	2.50	3.41	2.59	2.97	3.49	3.00	3.71	2.77	3.51	3.53	2.89	2.92	3.18	3.12	2.68	3.34	3.00	1.72
P ₂ O ₅	0.28	0.39	0.28	0.34	0.41	0.34	0.42	0.31	0.38	0.41	0.44	0.44	0.49	0.50	0.43	0.53	0.49	0.30
MnO	0.18	0.19	0.18	0.19	0.17	0.19	0.18	0.19	0.19	0.18	0.16	0.15	0.14	0.15	0.14	0.15	0.15	0.18
LOI	1.00	0.64	1.05	-0.05	0.24	0.39	0.96	0.81	0.56	0.05	0.98	3.18	1.99	1.61	3.14	1.58	2.24	2.28
H ₂ O ⁺	0.42	0.48	0.84	0.82	0.77	0.32	0.55	0.54	0.04	0.64	0.50	0.68	0.74	0.49	0.86	0.72	0.62	0.30
Total	100.52	99.80	100.81	100.42	99.82	100.58	99.24	100.05	99.64	99.05	100.13	100.27	100.46	99.10	100.31	99.81	100.20	100.43
Mg-no.	52	44	53	49	48	47	46	42	44	48	73	73	74	73	76	73	77	79
Trace elements (ppm)																		
Rb	19	18	22	13	26	36	29	22	21	17	18	31	31	29	47	37	29	13
Ba	265	394	258	249	379	320	530	1407	365	334	587	559	1051	1245	706	1115	948	248
Th	2.23	3.18	2.05	2.08	2.67	2.67	3.35		3.17	2.58	2.53		4.65	4.11	2.55	4.92	4.84	1.62
Nb	16.07	20.22	15.44	12.44	14.58	13.50	17.67	11.40	24.40	15.54	11.80	15.70	15.25	13.15	9.47	16.68	26.68	16.04
Sr	410	505	425	440	643	471	647	379	480	508	886	917	1068	1355	811	1161	1043	405
Hf	5.29	6.82	5.22	5.99	7.69	6.63	7.52		6.95	7.36	7.00		10.52	9.71	8.51	11.21	10.71	3.63
Zr	205	252	246	222	336	296	288	204	267	271	304	307	399	371	332	438	422	134
Y	29.6	36.8	29.1	30.9	41.7	30.7	40.8	38.5	37.1	34.8	22.4	27.5	24.2	25.7	22.6	25.3	22.8	14.7
Pb	3.04	5.82	2.85	2.89	3.79	3.70	5.16		4.26	3.53	3.93		7.36	7.57	5.12	7.90	6.84	2.88
Ta	1.07	1.30	1.02	1.22	1.44	5.58	1.23		1.71	2.23	1.16		1.73	1.24	0.99	1.52	3.25	1.21
U	0.46	0.68	0.45	0.49	0.65	0.59	0.70		0.70	0.62	0.53		0.92	0.85	0.52	0.98	1.03	0.34
Sc	32	31	30	31	24	36	27	35	29	28	21	20	29	21	19	21	16	10

V	359	412	357	359	348	410	362	411	413	406	235	234	242	252	203	248	199	152
Cr	162	78	159	87	128	84	63	149	62	98	1028	899	960	886	920	857	879	1292
Co	41	43	43	45	46	44	43	41	44	41	66	60	63	61	59	61	67	90
Ni	101	53	105	75	110	68	83	80	80	69	710	634	694	603	715	641	837	954
La	22.97	31.80	22.42	21.94	27.86	25.33	33.38		33.81	27.98	32.02		72.41	51.50	37.07	76.68	73.43	16.85
Ce	54.56	76.78	53.60	61.06	80.53	71.09	78.17		74.45	81.72	81.12		132.79	114.82	85.77	143.53	138.52	37.19
Pr	7.39	10.26	7.33	7.28	9.13	7.70	10.88		10.43	9.11	9.37		17.49	15.25	11.37	18.62	17.60	4.84
Nd	29.56	42.86	30.65	33.41	42.00	38.77	45.94		42.20	41.54	47.31		71.31	66.92	51.63	78.32	73.29	21.92
Sm	7.25	10.10	7.21	8.04	9.94	9.01	10.61		9.79	9.71	10.42		13.40	12.96	10.94	14.25	13.07	5.07
Eu	2.08	2.74	2.12	2.55	3.13	2.77	2.96		2.72	3.01	2.83		3.61	3.61	3.05	3.82	3.50	1.63
Gd	6.71	9.00	6.56	6.16	7.10	6.28	10.13		9.20	6.94	10.26		11.04	10.95	9.07	11.73	10.76	3.85
Tb	0.98	1.24	0.96	1.11	1.34	1.12	1.39		1.23	1.30	1.04		1.18	1.20	1.05	1.25	1.13	0.60
Dy	5.25	6.90	5.15	6.77	7.96	7.41	7.47		6.59	7.69	5.92		6.06	6.31	5.57	6.37	5.76	3.39
Ho	1.12	1.37	1.07	1.19	1.40	1.23	1.48		1.37	1.34	0.95		0.97	1.02	0.90	1.01	0.92	0.58
Er	2.89	3.52	2.73	3.39	3.87	3.76	3.81		3.63	3.75	2.38		2.49	2.63	2.36	2.63	2.38	1.59
Yb	2.59	3.08	2.44	2.77	3.08	3.15	3.19		3.07	2.98	1.82		1.81	1.93	1.72	1.90	1.72	1.23
Lu	0.37	0.45	0.34	0.37	0.41	0.40	0.45		0.45	0.40	0.24		0.24	0.25	0.22	0.25	0.22	0.17

Group type:	Lava flows and sills (high-Ti)								Lava flows and sills (low-Ti)							
Location:	Northern Botswana			Tuli (B)			W of Tuli (S)	Southern Botswana	Northern Botswana			W of Tuli (S)	Southern Botswana			
Sample type:	Lava flow						Plug	Sill	Lava flow						Sill	
Depth (m)	−763.8	−141.0						379.0	−112.2	−825.0	−488.4		−154.3	−103.5	−719.0	−355.1
Sample no.:	Maun-5	P11-2	Bo10	Bot0016	Bo27	Bo30	Bo32	Ckp8C1-2	Ckp11-11	Maun-7	P11-19	Bo2	C7-2	Ckp6-2	S719	Ckp8A1

Major elements (wt%)

SiO ₂	51.61	52.17	49.84	49.61	50.75	49.02	50.55	48.93	50.25	49.66	50.65	50.01	49.28	49.52	49.66	51.96
Al ₂ O ₃	13.16	13.82	12.52	13.73	13.70	11.90	13.53	12.38	14.79	14.05	14.87	15.00	15.44	14.51	15.24	13.31
Fe ₂ O ₃	12.33	11.74	13.28	13.37	11.94	13.30	14.13	14.09	10.58	12.91	10.59	11.23	10.74	10.43	10.97	15.24
MgO	3.58	4.04	4.80	6.39	4.68	6.78	5.53	8.57	7.30	6.04	6.68	6.27	7.66	6.92	6.13	4.52
CaO	7.93	7.33	8.72	10.50	7.96	8.93	9.58	9.92	10.61	10.63	10.63	10.48	10.58	8.46	10.57	8.82
Na ₂ O	2.36	2.91	2.47	2.38	2.60	2.18	2.38	2.15	2.33	2.16	2.12	2.34	2.60	4.04	2.80	2.73
K ₂ O	2.00	2.00	0.86	0.39	2.03	1.66	0.79	0.50	0.52	0.23	0.31	0.79	0.46	0.93	0.74	1.03
TiO ₂	3.85	2.91	3.89	2.58	3.50	3.52	3.29	1.99	0.96	1.17	0.91	0.98	0.89	0.87	1.07	1.71
P ₂ O ₅	0.65	0.65	0.58	0.29	0.54	0.42	0.38	0.21	0.15	0.16	0.14	0.17	0.12	0.14	0.18	0.26
MnO	0.13	0.15	0.18	0.20	0.14	0.15	0.18	0.19	0.19	0.18	0.18	0.18	0.15	0.16	0.21	0.23
LOI	0.90	1.60	1.40	0.18	0.79	0.56	0.04	0.74	1.21	2.18	2.12	1.22	0.81	2.64	1.49	0.49
H ₂ O [−]	1.60	0.57	0.80	0.48	0.74	0.75	0.40	0.24	1.33	1.29	1.32	1.28	1.22	1.05	0.84	0.39
Total	100.08	99.89	99.34	100.10	99.37	99.17	100.78	99.91	100.22	100.66	100.52	99.95	99.95	99.67	99.90	100.69
Mg-no.	40	45	46	53	48	54	48	59	62	52	60	57	62	61	57	41

Group type:	Lava flows and sills (high-Ti)								Lava flows and sills (low-Ti)										
Location:	Northern Botswana			Tuli (B)			W of Tuli (S)	Southern Botswana	Northern Botswana			W of Tuli (S)	Southern Botswana						
Sample type:	Lava flow						Plug	Sill	Lava flow						Sill				
Depth (m)	−763.8		−141.0					379.0	−112.2		−825.0		−488.4			−154.3	−103.5	−719.0	−355.1
Sample no.:	Maun-5	P11-2	Bo10	Bot0016	Bo27	Bo30	Bo32	Ckp8C1-2	Ckp11-11	Maun-7	P11-19	Bo2	C7-2	Ckp6-2	S719	Ckp8A1			
Trace elements (ppm)																			
Rb	30	33	18	6	27	32	19	10	11	2	3	17	8	25	11	24			
Ba	961	946	341	231	824	638	364	170	134	100	147	198	132	240	207	331			
Th	6.30	6.33	2.38	1.63	5.02	3.92	2.60	1.41	0.80	1.19	0.80	1.41	0.80	0.98	1.33	2.93			
Nb	29.80	27.02	12.71	8.74	22.32	17.64	11.85	7.87	3.94	4.90	4.51	7.40	4.30	4.94	7.28	9.17			
Sr	1006	1036	661	449	925	739	579	352	218	198	204	200	206	279	194	193			
Hf	13.11	10.85	5.61	4.86	9.78	8.79	7.43	3.94	1.94	2.47	1.81	2.73	1.78	2.20	8.60	4.33			
Zr	498	409	224	209	360	329	280	135	67	88	65	98	59	101	104	151			
Y	50.2	41.8	42.0	28.4	37.1	37.5	36.1	28.5	22.1	27.9	21.8	25.7	20.0	19.4	27.0	41.1			
Pb	10.78	9.31	6.29	2.59	9.95	6.68	3.67	2.57	2.08	2.28	2.97	2.63	2.06	2.83	3.09	6.99			
Ta	1.89	1.79	0.86	0.88	1.50	1.19	1.22	0.52	0.54	0.49	0.57	2.58	0.58	1.58	0.59	0.55			
U	1.24	1.19	<0.5	0.41	0.92	0.69	0.61	0.31	0.18	0.27	0.24	0.29	0.19	0.77	0.26	0.57			
Sc	22	21	21	35	21	23	33	27	30	27	29	32	27	24	31	30			
V	259	209	303	387	266	254	360	302	237	259	221	239	197	231	251	299			
Cr	31	71	70	122	57	273	93	274	272	92	286	179	255	297	186	17			
Co	39	36	49	44	43	51	47	55	38	39	38	39	42	36	35	41			
Ni	73	44	79	81	72	175	98	238	75	59	89	63	91	80	61	28			
La	63.22	59.08	23.96	17.21	48.50	38.73		14.77	7.89	8.47	7.58	11.38	7.36	6.85	11.42	17.18			
Ce	145.74	138.15	55.84	47.93	107.22	87.83		34.45	17.08	20.57	17.16	24.08	15.95	15.20	25.21	40.24			
Pr	19.76	18.07	7.93	5.62	15.03	12.52		4.96	2.30	2.80	2.30	3.40	2.18	2.04	3.34	5.26			
Nd	78.69	71.27	33.13	28.95	59.77	51.44		21.21	10.10	12.02	9.78	13.57	9.31	9.89	13.83	21.14			
Sm	17.18	14.79	7.49	7.16	12.90	11.94		5.71	2.85	3.51	2.77	3.61	2.52	2.93	3.62	5.57			
Eu	4.70	4.09	2.08	2.12	3.60	3.23		1.69	0.98	1.10	0.85	1.12	0.84	1.00	1.11	1.58			
Gd	15.77	13.32	6.69	6.10	11.46	10.79		5.64	3.25	4.13	3.17	4.19	2.84	3.33	4.08	6.32			
Tb	1.98	1.67	0.89	1.01	1.44	1.43		0.87	0.54	0.70	0.51	0.67	0.47	0.53	0.63	1.01			
Dy	9.62	8.02	4.33	6.51	7.38	7.26		5.02	3.45										

This version of the table shows rocks analyzed for isotopic compositions only (compare Table 2). The complete dataset has been given as Electronic Appendix 1, which is available for downloading at <http://petrology.oxfordjournals.org>. LOI, loss on ignition; B, Botswana; Z, Zimbabwe; S, Serowe; Sabie m., Sabie monocline. Major and trace element data in italics were obtained by XRF; other trace element data were obtained by ICP-MS. GPS coordinates of individual samples are reported in Electronic Appendix 1.

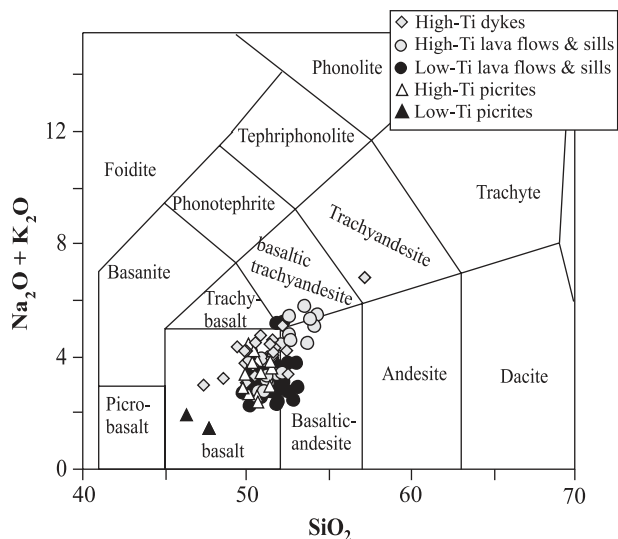


Fig. 3. Total alkali-silica diagram (TAS, Le Bas *et al.*, 1986).

exhibits a negative covariation with TiO_2 , P_2O_5 , and FeO_t (FeO_t not shown) and a positive covariation with CaO and Al_2O_3 (Fig. 4a), suggesting that these magmas have undergone low-pressure differentiation involving largely plagioclase and pyroxene.

The low-Ti basaltic lava flows ($n=32$) are classified as basalts with a few basaltic andesites, just as for the high-Ti dykes. Overall, the low-Ti basalts tend to be shifted towards higher Mg-number compared with the high-Ti basalts (Fig. 4a), indicating less evolved compositions. The two groups differ primarily in terms of their TiO_2 and P_2O_5 contents, and, for the low-Ti group, by the more limited range of these two elements for a given Mg-number.

The last group consists of mafic dykes and lava flows from the Letaba Formation, corresponding to the so-called picrites (Eales *et al.*, 1984; Ellam & Cox, 1989), which are restricted to the Tuli-Mwenezi-North Lebombo area. Although these rocks classify as basalts on the TAS diagram (Fig. 3), they will hereafter be referred to as 'picrites' according to previous studies and in agreement with their high MgO (12.7–17.6 wt %) and olivine contents. As for the basaltic lava flows, the picrites can also be divided into two subgroups defined on the basis of their TiO_2 contents, which range from 2.5 to 3.5 wt % for the widely dominant high-Ti group (nine samples from Tuli, two samples from Mwenezi, and two samples from Lebombo) and from 1.7 to 1.8 wt % for the less abundant low-Ti group (two samples deriving from rare intrusions within the Mwenezi high-Ti basalts). These rocks are characterized by high Mg-number (ranging from 71 to 77 and 79 to 82 for the high- and low-Ti groups, respectively). In the CaO and Al_2O_3 vs Mg-number plots (Fig. 4a), the high- and low-Ti picrites

define a negative covariation, indicative of either olivine fractionation or accumulation in the absence of clinopyroxene (or plagioclase) fractionation (as illustrated by the crystallization vectors in Fig. 4a; e.g. Albarède *et al.*, 1997; Peate *et al.*, 2003).

Trace elements

The high- and low-Ti groups also display contrasting trace element behaviours. The high-Ti basaltic lavas, sills, and dykes show large variations defining the following trends as a function of decreasing Mg-number (Fig. 4b): (1) decreasing concentrations of the compatible elements Ni and Cr, whereas V and Sc are more scattered (not shown); (2) increasing concentrations of the incompatible elements Th, La, Nb, Zr, Y, Ba, Rb, and Sr with more scatter among the large ion lithophile elements (LILE) such as Ba and Rb. The few N70° dykes analyzed lie within the compositional range of the N110° dykes. For very incompatible trace elements [VICE; e.g. light REE (LREE), Th, Nb, Zr], the high-Ti lava flows are subdivided into two groups forming two distinct trends (except for Yb and the more compatible trace elements) generally encompassing the range of the high-Ti dykes. These two groups will hereafter be referred to as the low incompatible trace element (low-ITE) and the high incompatible trace element (high-ITE) groups (Fig. 4b).

Chondrite-normalized REE patterns of the high-Ti dykes are variably LREE-enriched [La_n ranges from 48 to 211 and $(\text{La/Yb})_n$ from 3.3 to 12.3], and show slight negative Eu anomalies [$\text{Eu}/\text{Eu}^* = 0.80\text{--}0.93$ with $\text{Eu}^* = \sqrt{(\text{Sm} \times \text{Gd})}$], except for the more differentiated sample Bot0049, which has $\text{La}_n = 291$ and $\text{Eu}/\text{Eu}^* = 0.72$ (Fig. 5a). We cautiously note, however, that the small Eu anomalies could be due to overcorrection of the isobaric interference of BaO on Eu during ICP-MS analysis.

The high-Ti rocks are characterized by a significant fractionation of heavy REE (HREE) relative to middle REE (MREE), with the Sm/Yb_n ratio varying from 2.1 to 5.1. The primitive mantle-normalized trace element patterns also show variable incompatible element enrichment and negative Nb and Sr anomalies, except for sample Bo24, which exhibits a strong positive Sr anomaly as a result of plagioclase glomerocryst accumulation (Fig. 5b). Among the high-Ti lava flows, the low-ITE and high-ITE groups differ in terms of their REE patterns (Fig. 5a) and their normalized trace element patterns (Fig. 5b). The low-ITE group fits the less enriched patterns of the high-Ti dykes, whereas the high-ITE group displays more enriched patterns and stronger HREE fractionation [$(\text{Sm}/\text{Yb})_n = 4.5\text{--}5.2$]. Both lava groups have larger negative Nb anomalies [$\text{Nb}/\text{Nb}^* = 0.43\text{--}0.57$, with $\text{Nb}^* = \sqrt{(\text{K} \times \text{La})}$] than the high-Ti dykes ($\text{Nb}/\text{Nb}^* = 0.48\text{--}1.54$; Figs 4b and 5b).

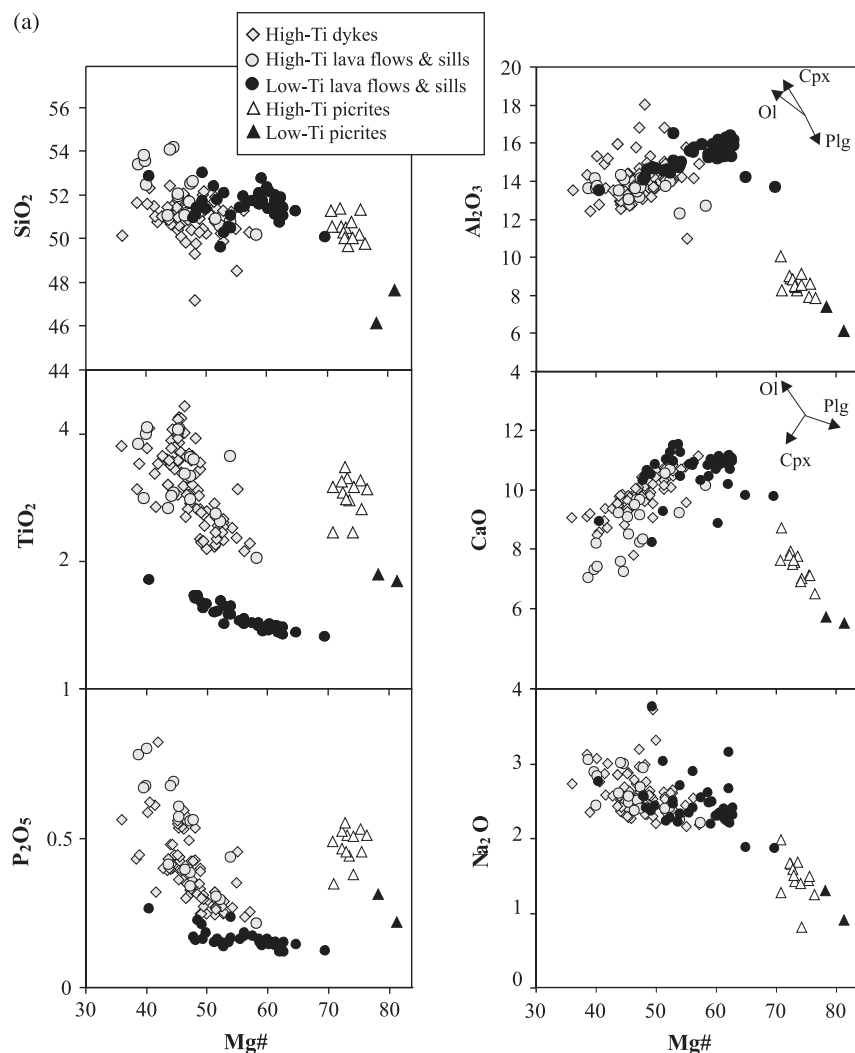


Fig. 4. (a) Selected major elements vs Mg-number [$100 \times \text{atomic ratio of Mg}/(\text{Mg} + \text{Fe}^{2+})$ with $\text{Fe}_2\text{O}_3/\text{FeO}$ normalized to 0.15]. The crystallization vectors of olivine, clinopyroxene, and plagioclase are indicated on the CaO and Al_2O_3 diagrams (see text for discussion). (b) Selected trace elements and Nb anomalies vs Mg-number. Nb/Nb^* corresponds to the Nb anomaly, with $\text{Nb}^* = \sqrt{(\text{K} \times \text{La})}$. Dotted fields indicate (when relevant) the high-ITE subgroup within the high-Ti lava flows and sills groups.

Compared with the high-Ti group, the low-Ti basaltic lava flows and sills have much less variable ITE abundances. They display a similar decrease and increase, respectively, in the abundances of compatible trace elements (Ni, Cr), HREE and Y, but a considerably smaller increase in VICE (e.g. Th, La, Nb, Zr), with decreasing Mg-number (Fig. 4b). Ratios such as Zr/Y are therefore much lower for the low-Ti (2.7–4.2) than for the high-Ti (5.7–10.7) group. Rubidium and, to a lesser extent, Ba show more scattered concentrations, whereas Sr contents decrease slightly with decreasing Mg-number, contrary to the high-Ti group. The REE patterns and normalized trace element patterns of the low-Ti group are more homogeneous and less enriched in LREE and other VICE [e.g. $(\text{La}/\text{Yb})_n = 2.0\text{--}3.4$ compared with 4.8–13.1

for the high-Ti group]. The low-Ti group also differs from the high-Ti group by having flatter MREE–HREE patterns [$(\text{Sm}/\text{Yb})_n = 1.2\text{--}1.6$]. The normalized trace element patterns display marked negative Nb anomalies ($\text{Nb}/\text{Nb}^* = 0.22\text{--}0.81$) broadly similar to those observed for the high-Ti lava flows, small negative Ti and Eu anomalies ($\text{Ti}/\text{Ti}^* = 0.66\text{--}0.93$ and $\text{Eu}/\text{Eu}^* = 0.82\text{--}1.02$), and variable Sr anomalies ranging from negative to positive ($\text{Sr}/\text{Sr}^* = 0.48\text{--}1.38$) depending on plagioclase removal or accumulation (Fig. 5b).

All the picrites have high contents of compatible trace elements, which decrease with decreasing Mg-number; nevertheless, the low-Ti picrites have the highest concentrations (e.g. Ni, Fig. 4b). VICE contents (except for Nb) for low- and high-Ti picrites are about the same as for

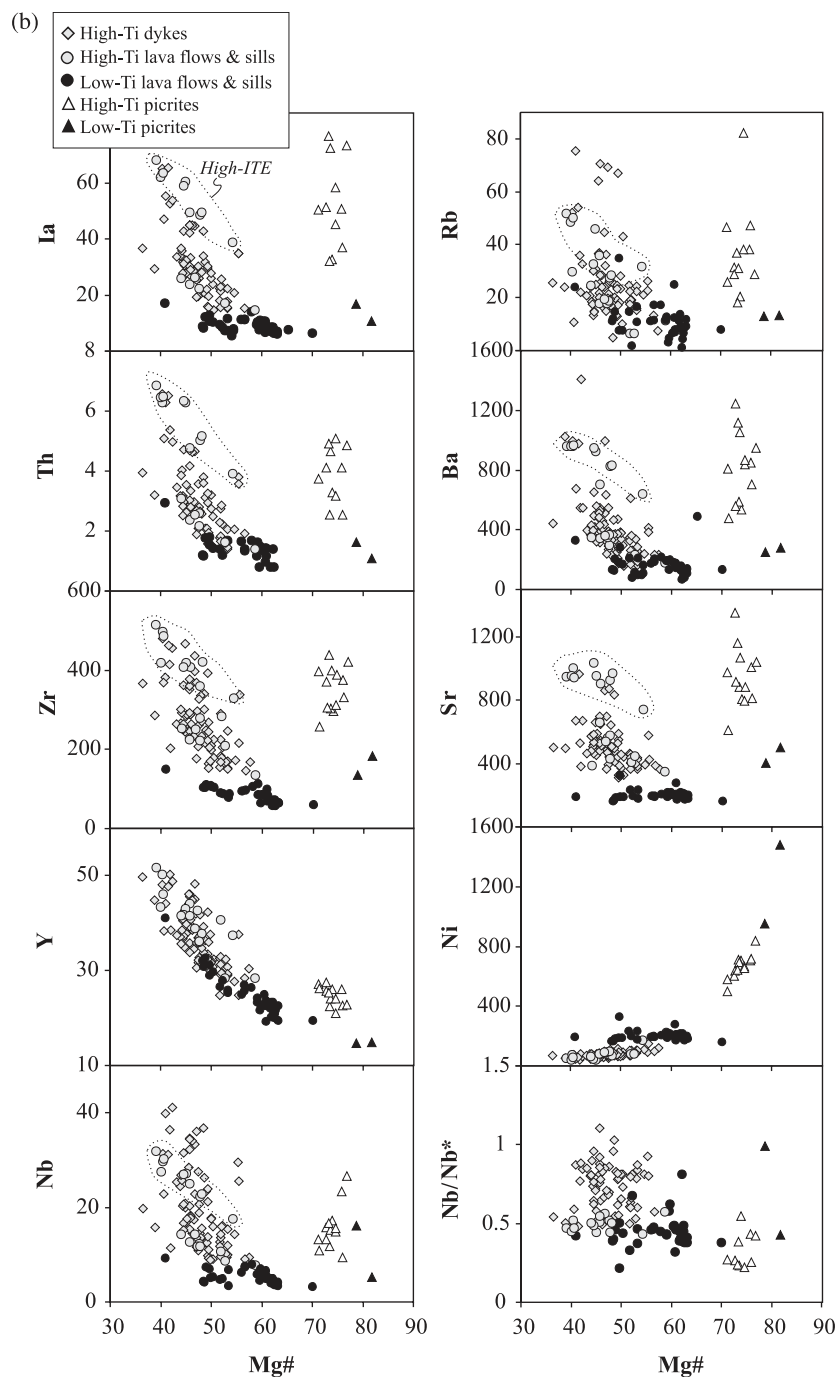


Fig. 4. Continued.

low- and high-Ti basalts with larger variations observed within the high-Ti groups, but no clear increase with decreasing Mg-number (Fig. 4b). The range for less incompatible elements such as Y (Fig. 4b) and HREE (not shown) is more restricted and lower for the high- and low-Ti picrites (22–28 and 14–15 ppmY) than for

the high- and low-Ti basalts (22–52 and 19–41 ppmY). As a result, the picrites display REE and multi-trace element patterns that are more fractionated than those of the basalts with higher MREE/HREE ratios [$(\text{Sm/Yb})_n = 6.0\text{--}8.1$ and $4.1\text{--}4.4$ for high- and low-Ti picrites, respectively]. The picrites also show negative Nb anomalies,

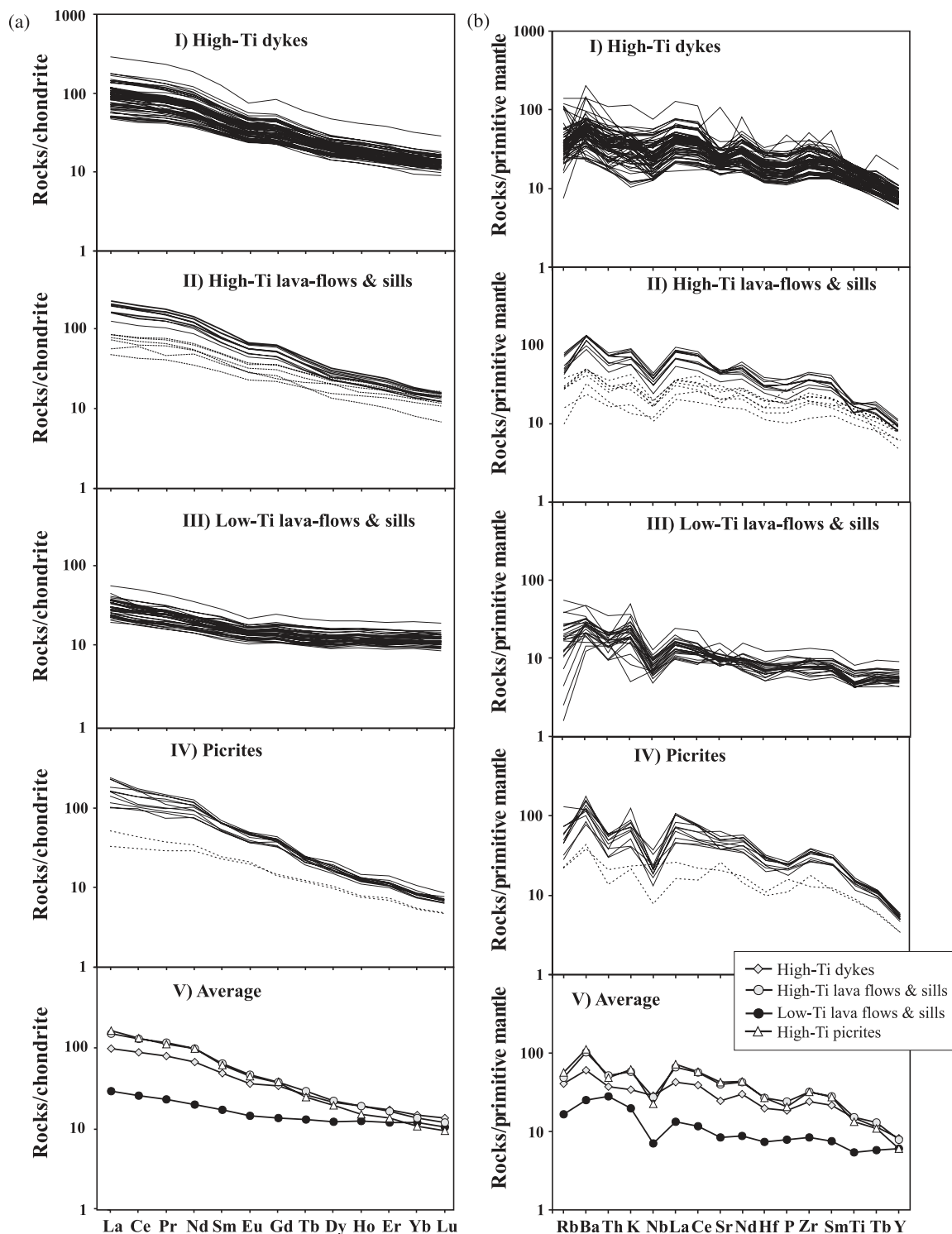


Fig. 5. (a) Chondrite-normalized (Boynton, 1984) REE patterns for the four Karoo groups: I, high-Ti dykes; II, high-Ti (continuous curves) and low-Ti (dashed curves) high-Ti lava flows and sills; III, low-Ti lava flows and sills; IV, high-Ti (continuous curves) and low-Ti (dashed curves) picrites; V, mean pattern for each group (symbols as in Fig. 3). (b) Primitive mantle normalized (Sun & McDonough, 1989) incompatible trace elements patterns for each group (I, II, III, IV, as above) and mean patterns (V).

with $\text{Nb}/\text{Nb}^* = 0.22\text{--}0.55$ and $0.43\text{--}0.99$ for the high- and low-Ti picrites, respectively. The negative Nb anomalies of the high-Ti picrites are among the largest observed in the present dataset.

Sr, Nd, Hf, and Pb isotopes

Ten high-Ti dykes from the Okavango dyke swarm, eight high-Ti lava flows, seven high-Ti picrites, and eight low-Ti lava flows were analyzed for their Sr, Nd, Hf, and Pb isotope compositions (Table 2 and Fig. 2). Additionally, one low-Ti picrite also was analyzed for its Nd and Hf isotope composition. Isotopic ratios were back-calculated to their initial values at 179 Ma in agreement with the $^{40}\text{Ar}/^{39}\text{Ar}$ ages determined by Le Gall *et al.* (2002) and Jourdan *et al.* (2004, 2005); these are the values reported in the various isotope plots (Fig. 6a–f). The samples show relatively large variations in $^{87}\text{Sr}/^{86}\text{Sr}_i$ (0.7040–0.7064), ϵNd_i (−9.4 to +1.1), ϵHf_i (−8.1 to +5.2), $^{206}\text{Pb}/^{204}\text{Pb}_i$ (16.62–18.02), $^{207}\text{Pb}/^{204}\text{Pb}_i$ (15.14–15.61), and $^{208}\text{Pb}/^{204}\text{Pb}_i$ (36.86–38.00) (Table 2), thus readily allowing discrimination of the four groups previously defined (Table 1 and Electronic Appendix 1).

The high-Ti dykes from the Okavango dyke swarm show a large range of Sr isotopic variation (0.7040–0.7059) for a restricted range of ϵNd_i (+1.1 to −2.2) and ϵHf_i (+1.3 to +5.2). On the ϵHf_i vs ϵNd_i plot (Fig. 6c) they lie along the mantle array (slope = 1.4, y-axis intercept = +3, J. Blichert-Toft, published and unpublished data compilation of ~2500 OIB and MORB of global distribution). In Pb–Pb isotope space (Fig. 6e and f), the dykes display relatively unradiogenic $^{206}\text{Pb}/^{204}\text{Pb}_i$ (17.15–17.62), unradiogenic to radiogenic $^{207}\text{Pb}/^{204}\text{Pb}_i$ (15.33–15.58), and moderately radiogenic $^{208}\text{Pb}/^{204}\text{Pb}_i$ (37.40–37.95) (for a given $^{206}\text{Pb}/^{204}\text{Pb}_i$ value). In the $^{207}\text{Pb}/^{204}\text{Pb}_i$ vs $^{206}\text{Pb}/^{204}\text{Pb}_i$ diagram (Fig. 6e), the high-Ti dykes plot to the left of the 179 Ma Geochron, extending from the Northern Hemisphere Reference Line (NHRL; Hart, 1984) toward compositions more radiogenic in ^{207}Pb and defining a steep positive slope parallel to the Geochron. $^{208}\text{Pb}/^{204}\text{Pb}_i$ is ‘decoupled’ from $^{206}\text{Pb}/^{204}\text{Pb}_i$, resulting in a clustering of the samples above the NHRL, between the Depleted MORB Mantle (DMM) and Enriched Mantle I (EMI) mantle components (Fig. 6f). This indicates moderately high time-integrated Th/Pb and a difference in the Th/U of the source(s) compared with the magma plotting on the NHRL. When $^{206}\text{Pb}/^{204}\text{Pb}_i$ is plotted against $^{87}\text{Sr}/^{86}\text{Sr}_i$, the samples fall between Bulk Silicate Earth (BSE) and EMI (Fig. 6d).

The high-Ti lava flows (except for sample Ckp8Cl-2, which displays both high- and low-Ti features) show a strong negative covariation between $^{87}\text{Sr}/^{86}\text{Sr}_i$ (0.7043–0.7057) and ϵNd_i (−0.2 to −7.8) (Fig. 6a). They define a marked trend from BSE toward and beyond the EMI-like component, in the direction of the Leucite Hills lamproite field (O’Briens *et al.*, 1995). Among these lava flow samples, the low-ITE subgroup plots close to BSE, whereas

the high-ITE subgroup corresponds to the enriched end-member of the trend. Similar relationships are observed in plots of ϵHf_i – ϵNd_i , $^{87}\text{Sr}/^{86}\text{Sr}_i$ – $^{206}\text{Pb}/^{204}\text{Pb}_i$, and ϵNd_i – $^{206}\text{Pb}/^{204}\text{Pb}_i$. The high-Ti lavas partially overlap with the high-Ti dykes in Pb–Pb isotope space (Fig. 6e and f), although they show slightly less radiogenic and more variable ratios ($^{206}\text{Pb}/^{204}\text{Pb}_i$ from 16.62 to 17.41, $^{207}\text{Pb}/^{204}\text{Pb}_i$ from 15.22 to 15.43, and $^{208}\text{Pb}/^{204}\text{Pb}_i$ from 37.10 to 37.58).

The low-Ti lava flows show more radiogenic $^{87}\text{Sr}/^{86}\text{Sr}_i$ (0.7053–0.7063) at similar ϵHf_i (−1.7 to +1.8) and ϵNd_i (−3.6 to −0.7) compared with the high-Ti dykes. In the ϵNd_i vs $^{87}\text{Sr}/^{86}\text{Sr}_i$ diagram (Fig. 6a), they extend the trend of the high-Ti dykes towards more radiogenic Sr isotope ratios, at similar ϵNd_i . A noteworthy feature is the presence of one outlier (Ckp8Al), which has more radiogenic $^{87}\text{Sr}/^{86}\text{Sr}_i$ (0.7073) for a similar ϵNd_i , apparently related to its evolved character (Mg-number = 41). Compared with the high-Ti group, the low-Ti lavas (1) have higher $^{206}\text{Pb}/^{204}\text{Pb}_i$ (17.60–18.02) for a similar range in $^{207}\text{Pb}/^{204}\text{Pb}_i$ (15.34–15.56) and $^{208}\text{Pb}/^{204}\text{Pb}_i$ (36.86–37.68), thus shifting them to the right of the Geochron (Fig. 6e and f), and (2) define opposite ‘trends’ in the ϵNd_i and $^{87}\text{Sr}/^{86}\text{Sr}_i$ vs $^{206}\text{Pb}/^{204}\text{Pb}_i$ diagrams (Fig. 6b and d).

The high-Ti picrites share some features with the high-ITE subgroup of the high-Ti lava flows, but extend to more enriched isotopic compositions with even lower ϵHf_i (−5.2 to −8.1) and ϵNd_i (−5.0 to −9.4) (Fig. 6a–c), locating them close to the field defined by the Leucite Hills and Gaussberg lamproites (O’Brien *et al.*, 1995; Murphy *et al.*, 2002, J. Blichert-Toft & B. Hanan, unpublished data). In the ϵHf_i vs ϵNd_i plot (Fig. 6c), the picrites (and possibly the high-ITE, high-Ti lava flows) define a shallower trend (slope = 0.6) than observed for the other high-Ti rocks, thus deviating slightly from the mantle (MORB–OIB) array. In Pb–Pb isotope space, the picrites overlap the fields of both high-Ti lava flows and dykes, defining an array parallel to (and to the left of) the Geochron (Fig. 6e). In the ϵHf_i vs ϵNd_i plot, the low-Ti picrite plots slightly below the mantle array, but has a composition similar to the high-Ti picrites.

Pb and Sr isotopic data for the high-Ti samples Bot0098 (Okavango dyke) and P11-2 (lava flow) were obtained for both the whole-rock and plagioclase separates (Table 2). For sample Bot0098, plagioclase, compared with the whole-rock, has slightly more radiogenic $^{206}\text{Pb}/^{204}\text{Pb}$, $^{207}\text{Pb}/^{204}\text{Pb}$, and $^{208}\text{Pb}/^{204}\text{Pb}$ and noticeably less radiogenic $^{87}\text{Sr}/^{86}\text{Sr}$ (Fig. 6d–f). For sample P11-2, plagioclase has overall less radiogenic Pb isotope compositions and less radiogenic $^{87}\text{Sr}/^{86}\text{Sr}$. The deviation between the Pb isotope compositions of the whole-rocks and the plagioclase separates is within (or slightly larger than) the error bars (Table 2), whereas the discrepancies observed for $^{87}\text{Sr}/^{86}\text{Sr}$ are significantly larger than what can be accounted for by the expected analytical

Table 2: Measured and initial (at 179 Ma) Sr, Nd, Hf, and Pb isotopic compositions of basaltic and picritic dykes, lavas, and sills from the Karoo province in Botswana and Zimbabwe

Sample	$^{87}\text{Sr}/^{86}\text{Sr}$	$^{87}\text{Sr}/^{86}\text{Sr}_i$	$^{143}\text{Nd}/^{144}\text{Nd}$	$^{143}\text{Nd}/^{144}\text{Nd}_i$	$\varepsilon(\text{Nd})_i$	$^{176}\text{Hf}/^{177}\text{Hf}$	$^{176}\text{Hf}/^{177}\text{Hf}_i$	$\varepsilon(\text{Hf})_i$	$^{206}\text{Pb}/^{204}\text{Pb}$	$^{206}\text{Pb}/^{204}\text{Pb}_i$	$^{207}\text{Pb}/^{204}\text{Pb}$	$^{207}\text{Pb}/^{204}\text{Pb}_i$	$^{208}\text{Pb}/^{204}\text{Pb}$	$^{208}\text{Pb}/^{204}\text{Pb}_i$
Okavango dyke swarm (high-Ti)														
<i>Shashe River</i>														
Bot0039	0.706233 ± 17	0.705889	0.512470 ± 15	0.512296	-2.2	0.282740 ± 8	0.282707	1.6	17.459 ± 16	17.197	15.437 ± 20	15.424	38.197 ± 37	37.780
Bot0060'	0.705061 ± 47	0.704806	0.512480 ± 18	0.512313	-1.8	0.282752 ± 8	0.282720	2.1	17.488 ± 30	17.247	15.352 ± 19	15.340	37.831 ± 77	37.492
Bot0065	0.704397 ± 16	0.704010	0.512522 ± 16	0.512355	-1.0	0.282765 ± 7	0.282734	2.6	17.480 ± 67	17.208	15.347 ± 63	15.334	38.019 ± 162	37.612
Bot0072	0.704437 ± 24	0.704214	0.512633 ± 14	0.512463	1.1	0.282816 ± 7	0.282786	4.4	17.917 ± 17	17.620	15.564 ± 17	15.549	38.327 ± 39	37.914
Bot0074	0.704487 ± 12	0.704178	0.512591 ± 14	0.512423	0.3	0.282806 ± 6	0.282780	4.2	17.834 ± 18	17.534	15.594 ± 17	15.579	38.356 ± 45	37.951
Bot0091	0.705435 ± 10	0.704866	0.512500 ± 17	0.512335	-1.4	0.282760 ± 5	0.282732	2.5	17.581 ± 20	17.304	15.474 ± 19	15.460	38.225 ± 52	37.814
Bot0098	0.706260 ± 34	0.705808	0.512498 ± 14	0.512335	-1.4	0.282780 ± 7	0.282735	2.6	17.388 ± 33	17.155	15.377 ± 38	15.365	37.815 ± 90	37.448
Bot0098 (pl)	0.704467 ± 14	0.704461							17.237 ± 18	17.237	15.404 ± 16	15.404	37.593 ± 38	37.593
Bo19	0.705520 ± 24	0.705200	0.512477 ± 19	0.512312	-1.9	0.282728 ± 7	0.282697	1.3	17.483 ± 15	17.199	15.424 ± 13	15.410	38.110 ± 31	37.687
<i>Maun</i>														
Bo52	0.705368 ± 23	0.704941	0.512555 ± 19	0.512398	-0.2	0.282838 ± 7	0.282807	5.2	17.618 ± 26	17.377	15.358 ± 22	15.346	37.740 ± 50	37.401
<i>Tuli (Zimbabwe)</i>														
Z1	0.704539 ± 26	0.704296	0.512524 ± 23	0.512358	-1.0	0.282788 ± 6	0.282762	3.6	17.676 ± 21	17.372	15.430 ± 21	15.415	37.998 ± 54	37.583
Picrite (high-Ti)														
<i>Tuli (Botswana)</i>														
Bo38	0.705350 ± 18	0.705200	0.512308 ± 13	0.512152	-5.0	0.282530 ± 6	0.282514	-5.2	17.390 ± 35	17.158	15.342 ± 35	15.330	37.772 ± 87	37.409
Bo39	0.706589 ± 10	0.706440	0.512268 ± 12	0.512112	-5.8	0.282525 ± 5	0.282508	-5.4	17.705 ± 23	17.462	15.539 ± 24	15.527	38.278 ± 56	37.935
<i>Tuli (Zimbabwe)</i>														
Z4	0.705276 ± 8	0.705060	0.512058 ± 10	0.511924	-9.4	0.282456 ± 6	0.282445	-7.3	17.264 ± 65	17.049	15.427 ± 68	15.416	38.074 ± 121	37.716
Z5	0.705610 ± 42	0.705454	0.512111 ± 10	0.511974	-8.5	0.282470 ± 5	0.282458	-7.2	17.302 ± 58	17.314	15.396 ± 53	15.498	37.607 ± 107	37.454
Z6	0.705526 ± 24	0.705324	0.512101 ± 24	0.511974	-8.5	0.282443 ± 8	0.282433	-8.1	17.025 ± 18	16.770	15.137 ± 13	15.124	37.422 ± 37	37.028
Z9	0.705903 ± 14	0.705470	0.512143 ± 13	0.511993	-8.2	0.282459 ± 5	0.282446	-7.6	17.378 ± 28	17.202	15.491 ± 28	15.483	38.016 ± 70	37.734
Z10	0.705413 ± 12	0.705180	0.512068 ± 13	0.511939	-9.2	0.282447 ± 6	0.282438	-7.9	17.370 ± 23	17.155	15.510 ± 25	15.499	38.047 ± 51	37.693

Picrite (low-Ti)*Mwenezi (Zimbabwe)*

Z30	—		0.512237 ± 15	0.512073	−6.5	0.282464 ± 7	0.282442	−7.8	—		—		—
-----	---	--	---------------	----------	------	--------------	----------	------	---	--	---	--	---

Lava flows (high-Ti)*North Botswana*

Bo10	0.704816 ± 17	0.704618	0.512387 ± 16	0.512227	−3.5	0.282667 ± 7	0.282649	−0.4	17.212 ± 17	16.965	15.313 ± 14	15.300	37.574 ± 34	37.186
P11-2	0.705577 ± 16	0.705345	0.512196 ± 14	0.512049	−7.0	0.282546 ± 5	0.282527	−4.7	16.961 ± 84	16.852	15.241 ± 96	15.235	37.434 ± 220	37.302
P11-2 (pl)	0.704597 ± 21	0.704591							16.615 ± 14	16.615	15.217 ± 14	15.217	37.096 ± 29	37.096
Maun-5	0.705052 ± 39	0.704834	0.512328 ± 18	0.512174	−4.6	0.282649 ± 6	0.282631	−1.0	17.081 ± 8	16.885	15.313 ± 8	15.303	37.595 ± 15	37.268

Tuli (Botswana)

Bot0016	0.704385 ± 14	0.704279	0.512566 ± 13	0.512390	−0.3	0.282802 ± 5	0.282765	3.7	17.684 ± 36	17.410	15.424 ± 29	15.410	37.942 ± 82	37.585
Bo27	0.705828 ± 14	0.705610	0.512159 ± 13	0.512006	−7.8	0.282544 ± 7	0.282525	−4.8	16.774 ± 29	16.618	15.290 ± 28	15.282	37.394 ± 66	37.114
Bo30	0.705785 ± 68	0.705469	0.512240 ± 16	0.512076	−6.5	0.282550 ± 6	0.282528	−4.7	17.073 ± 18	16.896	15.429 ± 15	15.420	37.846 ± 42	37.516

West of Tuli

Bo32	0.704537 ± 37	0.704300	0.512567 ± 13	0.512397	−0.2	0.282786 ± 4	0.282759	3.5	17.566 ± 16	17.280	15.373 ± 13	15.359	37.835 ± 61	37.434
------	---------------	----------	---------------	----------	------	--------------	----------	-----	-------------	--------	-------------	--------	-------------	--------

South Botswana

Ckp8C1-2	0.705939 ± 20	0.705720	0.512539 ± 17	0.512348	−1.2	0.282805 ± 8	0.282764	3.7	17.810 ± 26	17.599	15.559 ± 24	15.548	38.196 ± 48	37.882
----------	---------------	----------	---------------	----------	------	--------------	----------	-----	-------------	--------	-------------	--------	-------------	--------

Lava flows (low-Ti)*North Botswana*

Ckp11-11	0.706666 ± 18	0.706290	0.512574 ± 28	0.512370	−0.7	0.282796 ± 7	0.282713	1.8	18.059 ± 9	17.909	15.528 ± 10	15.521	37.692 ± 30	37.473
P11-19	0.706045 ± 21	0.705944	0.512487 ± 27	0.512286	−2.4	0.282784 ± 5	0.282698	1.3	18.159 ± 45	18.019	15.571 ± 50	15.564	37.794 ± 113	37.638
Maun-7	0.706207 ± 16	0.706148	0.512517 ± 23	0.512310	−1.9	0.282792 ± 11	0.282713	1.8	18.030 ± 52	17.824	15.352 ± 60	15.342	37.899 ± 145	37.601

South Botswana

C7-2	0.705915 ± 15	0.705631	0.512481 ± 24	0.512289	−2.3	0.282775 ± 6	0.282697	1.3	17.904 ± 19	17.746	15.346 ± 22	15.338	37.080 ± 44	36.861
------	---------------	----------	---------------	----------	------	--------------	----------	-----	-------------	--------	-------------	--------	-------------	--------

West of Tuli

Bo2	0.706486 ± 10	0.705850	0.512486 ± 24	0.512298	−2.1	0.282683 ± 7	0.282612	−1.7	18.122 ± 20	17.930	15.530 ± 19	15.521	37.991 ± 45	37.684
S719	0.706248 ± 16	0.705818	0.512456 ± 26	0.512270	−2.7	0.282704 ± 6	0.282682	0.7	17.728 ± 23	17.750	15.350 ± 19	15.397	37.716 ± 33	37.488
Ckp6-2	0.705973 ± 18	0.705317	0.512490 ± 23	0.512281	−2.5	0.282745 ± 8	0.282674	0.5	18.076 ± 20	17.606	15.456 ± 18	15.433	37.476 ± 41	37.280
Ckp8A1	0.708247 ± 16	0.707326	0.512408 ± 14	0.512221	−3.6	0.282710 ± 6	0.282643	0.6	18.126 ± 32	17.983	15.605 ± 31	15.598	38.239 ± 79	37.998

Errors (2σ) refer to the last decimal place.

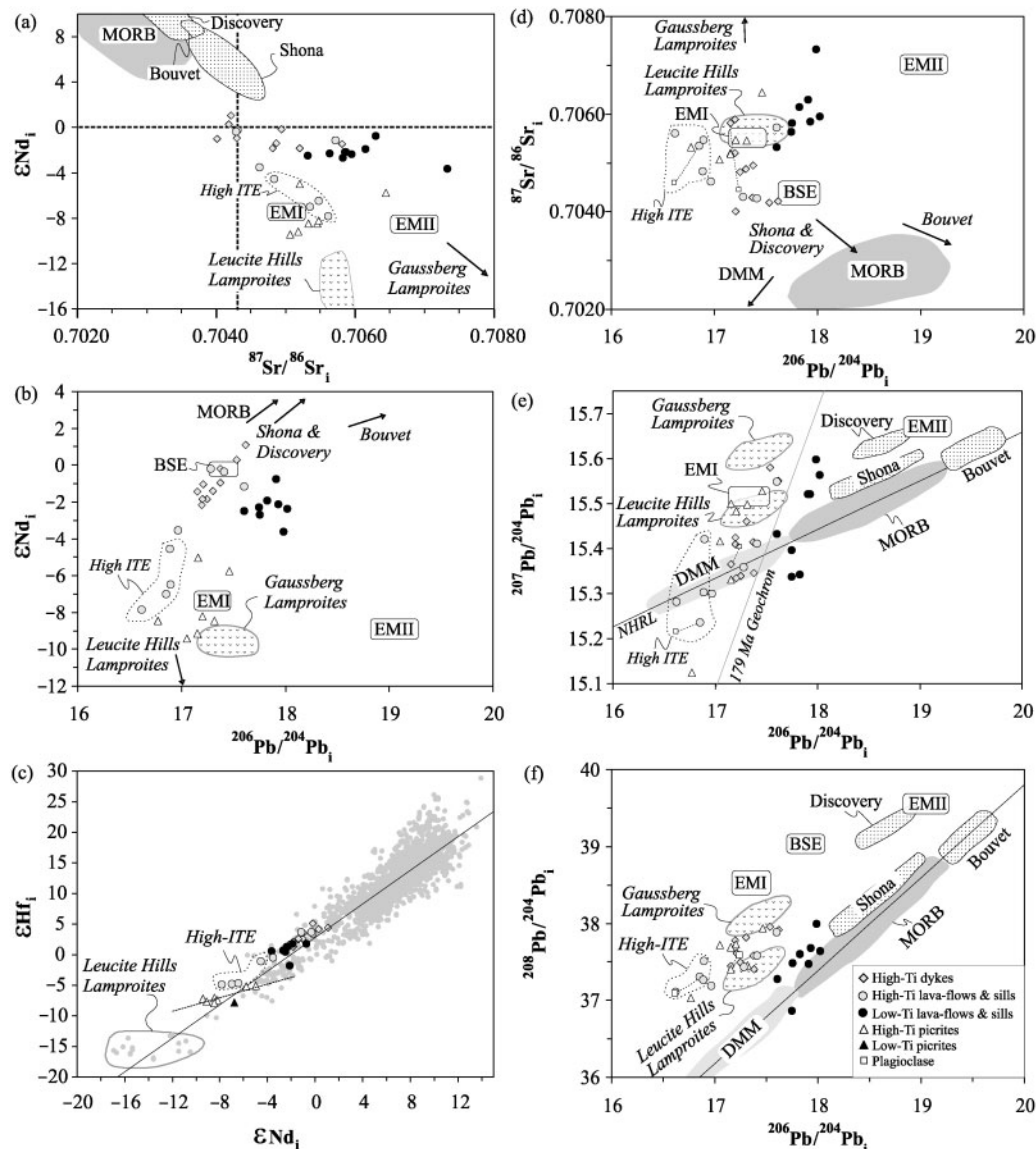


Fig. 6. Initial (at 179 Ma) Sr, Nd, Hf, and Pb isotopic compositions of the Botswana Karoo magmatic rocks and plagioclase separates from rocks Bot0098 and P11-2 (open squares linked to their respective whole-rocks by a tie-line). Initial Sr isotopic compositions of plagioclase have been calculated using 0.2 ppm Rb and 220 ppm Sr (estimated composition derived from Central Atlantic magmatic province plagioclase analyses, F. Jourdan, unpublished data). The initial Pb isotopic compositions of plagioclase are considered to be equal to the measured values as plagioclase has very high Pb/U and Pb/Th ratios. In Pb–Pb isotope space, the Northern Hemisphere Reference Line (NHRL; Hart, 1984) and Geochron at 179 Ma (Allègre *et al.*, 1988) are shown. Approximate locations of mantle end-members (Zindler & Hart, 1986) are indicated for reference. Also shown are the fields of selected plume-related South Atlantic Ocean islands [Bouvet (Sun, 1980); Discovery and Shona (Douglass *et al.*, 1999)], and the fields of the Leucite Hills (O'Brien *et al.*, 1995) and Gaussberg lamproites (Murphy *et al.*, 2002). ϵHf and ϵNd data for the MORB and OIB reference field are from published (too numerous to be cited here) and unpublished (J. Blichert-Toft) sources. Leucite Hills lamproites are from J. Blichert-Toft & B. Hanan (unpublished data). The regression lines for the mantle array (continuous line) and the picrites (dashed line) are $y = 1.4x + 2.8$ ($n \sim 2500$) and $y = 0.6x - 2.4$, respectively. Dotted fields indicate the high-ITE subgroup within the high-Ti lava flows and sills group.

uncertainties and suggest a possible contribution from alteration processes, as will be discussed further below.

Chemical stratigraphy

The chemical stratigraphy of the lava pile in Botswana was assessed from the 370 m thick volcanic succession of the P11

borehole (Fig. 2a), from which 21 basalts were sampled at regular depth intervals. Based on the variations of Mg-number, TiO_2 , Nb, and La/Yb as a function of depth through the P11 section, three sequences can be identified (Fig. 7). The lower part of the section (from 500 m to 280 m depth in the borehole) consists of low-Ti basalts

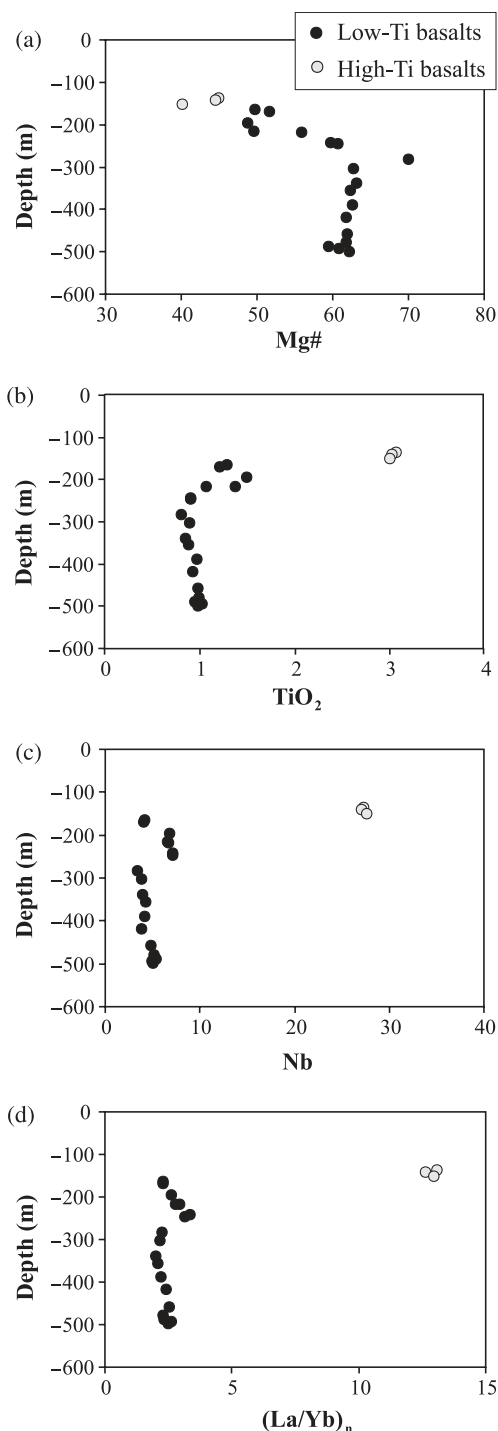


Fig. 7. Stratigraphic variation of Mg-number, TiO_2 , Nb, and $(\text{La}/\text{Yb})_n$ for the P11 borehole section.

displaying homogeneous compositions with subtle but regular variations of TiO_2 and Nb contents (0.85–1.02 wt % and 3.54–5.09 ppm, respectively) and trace element ratios [$(\text{La}/\text{Yb})_n = 2.00\text{--}2.61$]. These compositions are similar to those of other Karoo low-Ti stratigraphic

sequences (Cox, 1988; Sweeney *et al.*, 1994; Marsh *et al.*, 1997) and suggest the steady-state outpouring of magmas from a regularly replenished open magma chamber. An abrupt change occurs at the depth of 280 m, which is marked by the emplacement of a primary lava flow (Mg-number = 70) that shifts compositions towards higher Nb concentrations and La/Yb ratios and is in turn followed by a progressive decrease of these variables up to a depth of 160 m, whereas TiO_2 contents gradually increase. These small changes probably reflect the re-injection of a fresh pulse of undifferentiated magma that subsequently evolved by fractional crystallization processes. The most striking feature of the section is a dramatic shift within its uppermost 30 m (i.e. between depths of 160 and 130 m) of TiO_2 and Nb contents and La/Yb towards the significantly higher values diagnostic of the high-Ti magma group. These changes are broadly similar to those observed in some Lebombo (Sweeney *et al.*, 1994) and Springbok Flats (Marsh *et al.*, 1997) stratigraphic sequences. The switch from low- to high-Ti basalts is also marked by a change in isotopic composition [e.g. ϵNd_i decreases from -2.4 (P11-19) to -7.0 (P11-2)]. This abrupt stratigraphic shift from low- to high-Ti compositions likewise is observed in the P8 (close to the P11 borehole) and the Maun (northwestern Botswana) boreholes (Fig. 2a).

The sharp changes observed in major and trace element and isotopic compositions towards the top of the P11 borehole are inconsistent with progressive partial melting and differentiation processes being responsible for the low- to high-Ti transition, and rather suggest the tapping of two distinct magma sources as previously suggested by Cox (1988), Sweeney & Watkeys (1990), Sweeney *et al.* (1994) and Elburg & Goldberg (2000).

DISCUSSION

Alteration

In thin section, the effects of alteration on the rocks appear to be minor (especially for the samples selected for isotopic analysis) and, when optically discernible, mostly affect olivine (transformed into bowlingite). This observation is corroborated by the major and trace element compositions of the samples, which do not correlate with loss on ignition (LOI, not shown), suggesting that the rocks are unaltered. However, as mentioned above, the plagioclase and whole-rock isotopic compositions of samples Bot0098 and P11-2 show substantial differences for $^{87}\text{Sr}/^{86}\text{Sr}$ (Fig. 8), which suggest, on the contrary, a possible contribution from alteration. Effects of alteration are more likely to affect the Sr isotopic composition of the whole-rock than that of the separated plagioclase because (1) plagioclase was hand-picked under a binocular microscope, carefully selecting only the cleanest minerals, (2) the Bot0098 whole-rock is characterized by a large amount of a glassy

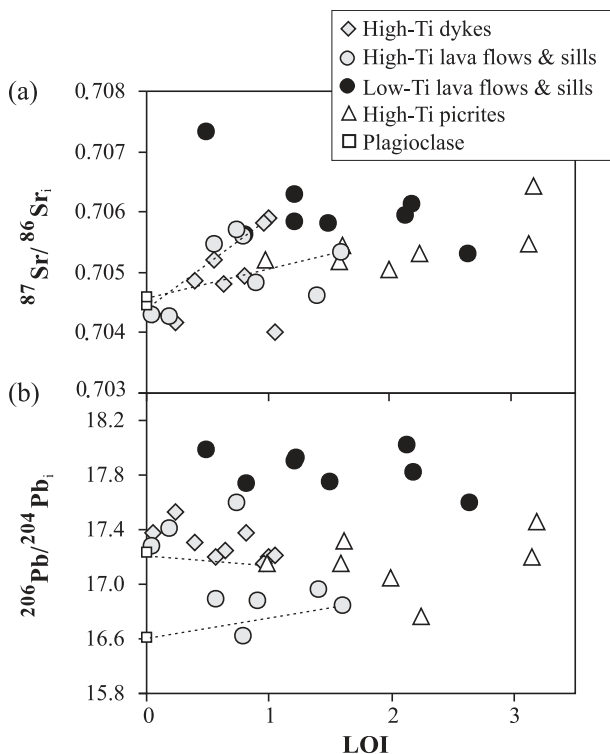


Fig. 8. Initial $^{206}\text{Pb}/^{204}\text{Pb}$ and $^{87}\text{Sr}/^{86}\text{Sr}$ vs. LOI. Plagioclase LOI is considered to be negligible.

oxidized groundmass, which is particularly sensitive to alteration, and (3) the Bot0098 whole-rock sample is shifted towards more radiogenic Sr (at a given ϵNd ; Fig. 6a) compared with other high-Ti dykes.

The isotope ratio vs. LOI plots show no visible covariation for Nd, Hf (not shown), or Pb (Fig. 8) isotopic compositions regardless of the group of rocks considered. In contrast, a positive correlation between $^{87}\text{Sr}/^{86}\text{Sr}$ and LOI is observed for the high-Ti dykes. This trend shows that (1) the less radiogenic samples have the same isotopic composition as the plagioclase separates from sample Bot0098 and (2) the trend is roughly parallel to the tie-line linking the Bot0098 whole-rock and plagioclase. This suggests that the high-Ti dykes are variably affected by alteration processes, with the samples with more radiogenic Sr being the most strongly affected (Fig. 8). Therefore, the variable $^{87}\text{Sr}/^{86}\text{Sr}$ compositions of the high-Ti dykes (Fig. 6) apparently do not reflect mantle source processes, but rather subsequent alteration (along with possible assimilation; see below). We propose that the pristine magmatic composition of the high-Ti dykes is more likely to be located near BSE (as suggested by their ϵNd values).

Similarly, the Sr isotopic composition also differs between the P11-2 whole-rock and fresh plagioclase separates. However, (1) the deviation is smaller than for

Bot0098, (2) the bulk high-Ti lava group does not show a clear $^{87}\text{Sr}/^{86}\text{Sr}$ –LOI correlation, and (3) in this group, Sr and Nd isotope compositions display a pronounced negative covariation, which cannot be attributed to alteration (Fig. 6a). Therefore, although alteration cannot be excluded, it does not seem to affect the Sr isotopic compositions of the high-Ti lava flows and sills significantly. Although mineral compositions would be required to more fully assess this issue (which is beyond the scope of the present study), alteration processes probably modified the Sr isotopic compositions of some of the high-Ti dykes, but the overall role of alteration appears to have been negligible for the remaining rocks and the other isotopic systems employed here.

Petrogenesis

The low- and high-Ti basaltic and picritic rocks display a wide range of major and trace element and isotopic compositions (Figs 3–6) suggesting that a number of distinct differentiation processes took place, involving partial melting, fractional crystallization, and possibly crustal contamination.

Partial melting

One of the key differences between the high- and low-Ti groups is their contrasting trace element patterns (Fig. 5), best illustrated by the MREE/HREE fractionation systematics (Fig. 9). Whereas LREE/MREE ratios (e.g. La/Sm) largely overlap between the two groups, the MREE/HREE ratios of the high-Ti samples are systematically higher and much more variable [e.g. $(\text{Sm}/\text{Yb})_n = 2.5\text{--}5.3$] than those of the low-Ti samples [$(\text{Sm}/\text{Yb})_n$ nearly constant at 1.2–1.6]. These ratios do not correlate with Mg-number and the variations clearly cannot be explained by fractional crystallization or crustal contamination processes. Rather, they indicate different depths of melting: the high-Ti basalts require significant amounts of garnet in their source to account for their high Sm/Yb ratios, whereas the less enriched, nearly flat Sm–Yb trend of the low-Ti basalts excludes the presence of garnet in their source and calls for melting of a shallower spinel-bearing source.

To evaluate the melting conditions, we used the standard equation of Shaw (1967) to model non-modal melting of a slightly LREE-enriched garnet-bearing lherzolite [$\text{La}_n = 4.4$; $(\text{La}/\text{Yb})_n = 2.02$] with a modal composition of 64–68% olivine, 20% orthopyroxene, 9% clinopyroxene, and 2–7% garnet. The observed patterns of the high-Ti rocks and picrites can be reproduced by equilibrium melting in the range of 2–8% for the dykes and low-ITE lava flows, 2.5–4% for the high-ITE lava flows, and 3–10% for the picrites (Fig. 9). The degrees of melting were calculated assuming that each group is derived from a homogeneous mantle source. If the source is not homogeneous, then part of the observed spread is not necessarily

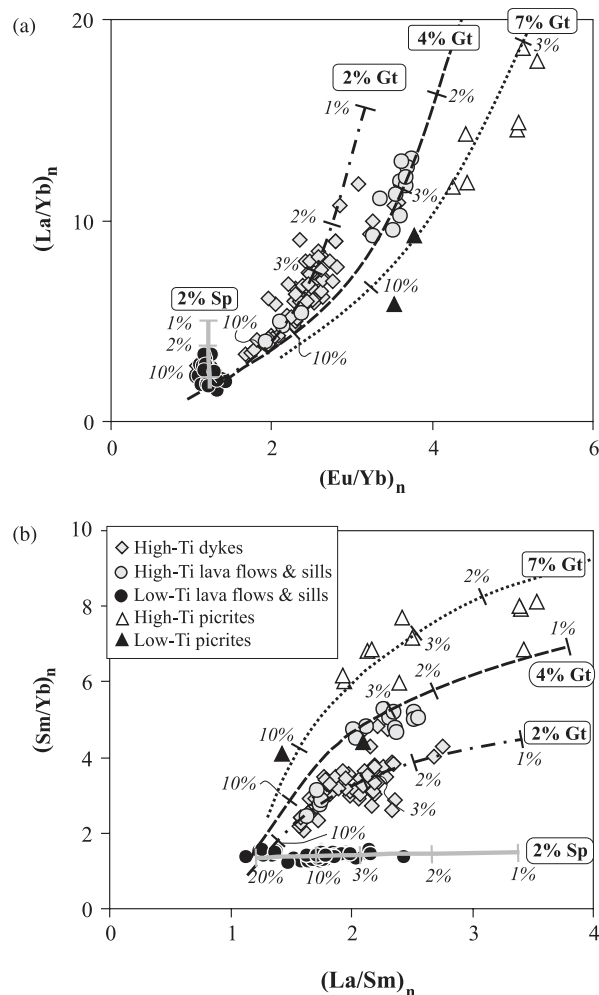


Fig. 9. $(\text{La}/\text{Yb})_n$ vs $(\text{Eu}/\text{Yb})_n$ and $(\text{Sm}/\text{Yb})_n$ vs $(\text{La}/\text{Sm})_n$ for the Botswana Karoo rocks and non-modal batch melting modeling of a lherzolitic mantle source. Values are chondrite-normalized after Boynton (1984). Partition coefficients are from McKenzie & O'Nions (1991). The tick marks on the curves correspond to melting degrees. Grey curve: melting curve of a spinel-bearing lherzolite source (modal composition: 55% olivine, 15% orthopyroxene, 28% clinopyroxene, and 2% spinel). Melting mode: 20% olivine, 20% orthopyroxene, 55% clinopyroxene, and 5% spinel. Source composition: 1.10 ppm La, 0.67 ppm Sm, 0.24 ppm Eu, and 0.55 ppm Yb. Black curves: melting curves of garnet-bearing lherzolite mantle sources containing 2% (dashed-dotted), 4% (dashed), and 7% (dotted) modal garnet, respectively. Source modal composition range: 69–64% olivine, 20% orthopyroxene, 9% clinopyroxene, and 2–7% garnet. Melting mode modified from Walter (1998): 16% olivine, 12% orthopyroxene, 81% clinopyroxene, and 15% garnet. Source composition: 1.35 ppm La, 0.62 ppm Sm, 0.19 ppm Eu, and 0.45 ppm Yb.

due to petrogenetic processes. Figure 6 shows that most groups lie along mixing trends, potentially indicating source heterogeneity. Therefore, the ranges of degrees of melting indicated above are likely to be maximum values for each group. The different levels of MREE/HREE enrichment are better explained by variable amounts of garnet in the mantle

source, from 2% (Okavango dyke swarm and low-ITE lavas) to 4% (high-ITE lavas) and 7% (picrites). This would indicate that the picrites and (to a lesser extent) the high-ITE lava flows derive from deeper levels in the mantle than the dykes, thus precluding that the Okavango dyke swarm could be a feeder system to the high-Ti lava flows.

To explain the flatter MREE–HREE patterns of the low-Ti lava flows, we modeled non-modal equilibrium melting of a spinel-bearing lherzolite with 55% olivine, 15% orthopyroxene, 28% clinopyroxene, 2% spinel, and a slightly more LREE-enriched REE element pattern [$\text{La}_n = 3.5$; $(\text{La}/\text{Yb})_n = 1.35$] than that of the corresponding garnet-bearing source. The calculated melts, produced in the range of 2–20% melting, adequately match the observed REE variations (Fig. 9). As for the high-Ti groups, the calculated degrees of melting are mode-dependent (i.e. assuming that the mantle source is homogeneous) and therefore provide maximum values. Our modeling implies that low- and high-Ti magmas were generated at different depths: shallow [~ 25 – 30 kbar (i.e. 80–100 km), Robinson & Wood, 1998] for the low-Ti magmas and deeper (> 25 – 30 kbar) for the high-Ti magmas.

The mantle sources used in the two cases discussed above have different modal and chemical compositions and may not be directly related to each other, which is in agreement with the observed isotopic heterogeneities and with previous findings (e.g. Cox, 1988; Hawkesworth *et al.*, 1984; Sweeney *et al.*, 1994).

Fractional crystallization

Petrographic observations and major element behavior suggest that both the low- and high-Ti suites are well matched with the fractionation of gabbroic assemblages (mainly augite and plagioclase with minor amounts of magnetite and olivine) as commonly inferred for CFBs. We tested this hypothesis using the MELTS code of Ghiorso & Sack (1995) to calculate the liquid lines of descent of the magmas and provide the composition of the residual liquid (Fig. 10) and the cumulate minerals (Fig. 11). We did isenthalpic runs using several sets of experimental conditions [$P = 1$ – 3 kbar, $\text{H}_2\text{O} = 0$ – 1% , and $f\text{O}_2 = \text{QFM}$ (quartz–fayalite–magnetite)]. Using one of the least differentiated samples, Bot02, as our starting composition, the high-Ti suite is best reproduced by up to 50 wt % of anhydrous and low-pressure (1 kbar) fractional crystallization of gabbroic assemblages comprising plagioclase (54 wt %), augite (22 wt %), pigeonite (16 wt %), and olivine (8 wt %). MELTS modeling predicts the following crystallization sequence (Fig. 11): plagioclase (An_{79-69}) \rightarrow olivine (Fo_{76-75}) + plagioclase (An_{67-65}) \rightarrow augite ($\text{Mg}_{41-38}\text{Ca}_{38-39}$) + pigeonite ($\text{Mg}_{53-50}\text{Ca}_{15}$) + plagioclase (An_{59-54}). This model provides the best fit to the chemical trends displayed by the high-Ti basaltic suite, but does not take into account earlier (and probably deeper-seated) fractionating assemblages because the

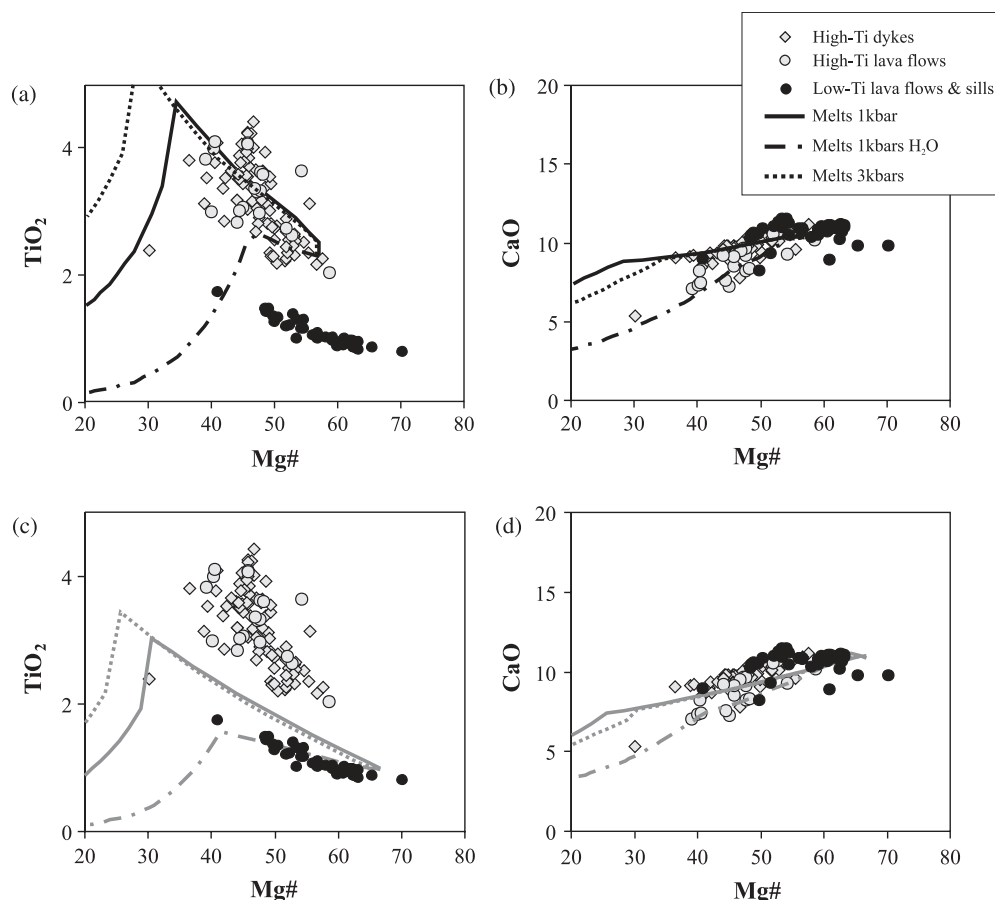


Fig. 10. TiO_2 and CaO vs Mg\# for the basaltic samples and MELTS (Ghiorso & Sack, 1995) fractional crystallization modeling curves. Calculation parameters: low pressure (1 kbar) and anhydrous (continuous curve); low pressure (1 kbar) and hydrous (1% H_2O) (dotted-dashed curve); moderate pressure (3 kbar) and anhydrous (dotted curve). A QFM buffer was used for $f\text{O}_2$. Models were run for both high-Ti rocks (a and b; starting composition: Bot02) and low-Ti rocks (c and d; starting composition: Ckpl1-7).

starting composition used here is not a primary magma. Therefore, the fractional crystallization amounts obtained by these calculations are likely to be minimum values.

Taking the more primitive sample Ckpl1-7 as starting composition and using the same conditions as for the high-Ti suite ($P=1$ kbar, $\text{H}_2\text{O}=0\%$), the low-Ti group can also be adequately matched, by up to 50 wt % fractional crystallization of gabbroic assemblages (48 wt % plagioclase, 22 wt % augite, 25 wt % pigeonite, and 5 wt % olivine). The crystallization sequence for the low-Ti suite is: plagioclase (An_{77}) + olivine (Fo_{81}) \rightarrow plagioclase (An_{79-69}) + olivine (Fo_{76-75}) + augite ($\text{Mg}_{41-38}\text{Ca}_{38-39}$) + pigeonite ($\text{Mg}_{53-50}\text{Ca}_{15}$).

In both cases, the MELTS modeling is in agreement with the observed parageneses, the mineral compositions as measured by electron microprobe (Wigley, 1995), and the geochemical data.

Crustal contamination

Although the major element trends can be reproduced by fractional crystallization modeling, the relatively large

range of isotopic compositions suggests additional contributions by contamination from lower and/or upper crustal sources.

In the $^{87}\text{Sr}/^{86}\text{Sr}$ and $^{208}\text{Pb}/^{204}\text{Pb}$ vs Mg\# plots (Fig. 12c and b), the low-Ti basalts show a negative covariation, which is in accordance with the slightly positive trend observed for these samples between $^{143}\text{Nd}/^{144}\text{Nd}$ and Mg\# (Fig. 12d) or SiO_2 content (not shown). However, no covariation is observed between $^{206}\text{Pb}/^{204}\text{Pb}$ and Mg\# (Fig. 12a). These observations suggest that the low-Ti basalts may have been contaminated by a component with radiogenic ^{87}Sr and ^{208}Pb , but 'normal' ^{206}Pb . A plausible contaminant would be the upper crust (e.g. Betton *et al.*, 1984), which may have readily interacted with the low-Ti magmas during their ascent. For some (but not all) of the high-Ti rocks, a negative covariation also is observed between $^{87}\text{Sr}/^{86}\text{Sr}$ and Mg\# (Fig. 12c), but in this case it is not mirrored by $^{208}\text{Pb}/^{204}\text{Pb}$ as a function of Mg\# (Fig. 12b), which instead correlate positively with each other. In addition, $^{143}\text{Nd}/^{144}\text{Nd}$ does not correlate with Mg\# (Fig. 12d).

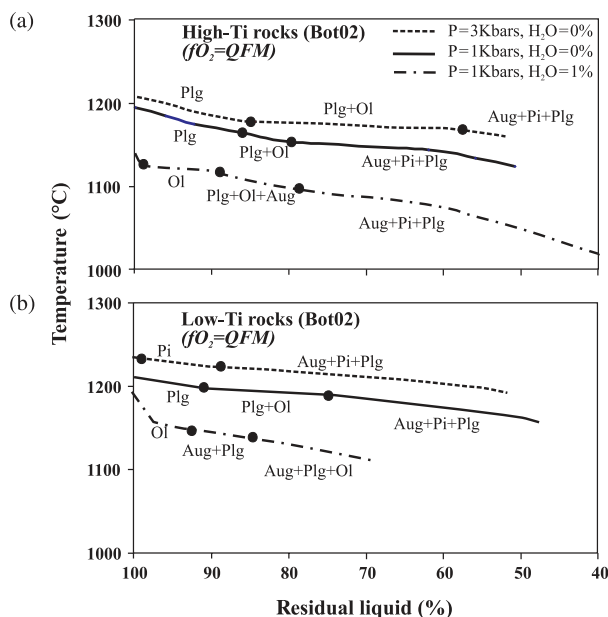


Fig. 11. Fractionating mineral assemblage and liquidus temperature calculated with MELTS for residual liquid percentage from starting compositions Bot02 (high-Ti group) and Ckpl1-7 (low-Ti group) under QFM conditions. Calculation run conditions as in Fig. 10.

Likewise, the high-Ti picrites (particularly sensitive to crustal contamination because of their ultramafic character) do not display clear relationships between their isotopic compositions and nearly constant Mg-number (~ 75), arguing against significant crustal assimilation. Thus, if the high-Ti group magmas were exposed to crustal contamination, then the contaminant was different from that affecting the low-Ti group, and possibly located in the lower crust.

To test further the possible influence of basement assimilation on both the low- and high-Ti groups, we used the energy-constrained assimilation and fractional crystallization (EC-AFC) model of Spera & Bohrsen (2001), applied to $^{208}\text{Pb}/^{204}\text{Pb}$ vs Pb and $^{87}\text{Sr}/^{86}\text{Sr}$ vs Sr (Fig. 13). Table 3 shows the thermal and geochemical input parameters employed. The thermal parameters are those used by Bohrsen & Spera (2001) for standard upper and lower crust. It is noteworthy that reasonable (100–200°C) variations in the temperature of the basement and its liquidus temperature, as well as the equilibration temperature of the bulk system, do not significantly influence the results. The composition of samples C7-2 and Bot0072 was taken as the starting value for the low- and high-Ti groups, respectively. The bulk Karoo rock compositions are plotted for comparison (Fig. 13).

The Pb and Sr elemental and isotopic compositions of the upper crustal contaminant are inferred based on the elemental and isotopic compositions of the strongly radiogenic Lebombo rhyolites, considered as a good proxy

for the local upper crust (Betton *et al.*, 1984). Neodymium isotopic compositions adopted for the upper crustal contaminant are those proposed by Bohrsen & Spera (2001). Resulting EC-AFC curves predict for both low- and high-Ti rocks a marked increase of $^{208}\text{Pb}/^{204}\text{Pb}$ (Fig. 13a) together with an increase in the Pb concentrations. Such behavior clearly is not shown by the high-Ti group, but fits well with the behavior of the low-Ti group. In the $^{87}\text{Sr}/^{86}\text{Sr}$ vs Sr plot (Fig. 13b), the model predicts increasing $^{87}\text{Sr}/^{86}\text{Sr}$ combined with slightly decreasing Sr concentrations for the contaminated magma, which is due to the compatible nature of Sr and the radiogenic composition of the upper crustal contaminant (Bohrson & Spera, 2001). Again, these anticipated trends are not observed for the high-Ti basalts, but fit, although to a limited extent, the low-Ti lava flows from Botswana. Compared with the Karoo Georoc database (Fig. 13b), our dataset for the high-Ti group covers most of the range of uncontaminated high-Ti Karoo samples, whereas our dataset for the low-Ti group is restricted exclusively to the lower part of the low-Ti Karoo reference field. This argues in favor of only limited influence of upper crustal contamination on our low-Ti sample suite (with the exception of the more differentiated lava flow Ckpl8A-1).

We chose granulitic orthogneisses from Antarctica (Antonini *et al.*, 1999) as representatives of the lower crustal contaminant because (1) no Pb isotopic data are available for southern Africa granulites, (2) they are in agreement with conventional Pb isotopic values for worldwide lower crust, and (3) they are close to the Sr isotopic compositions proposed by Bohrsen & Spera (2001) for the 'standard lower crustal case'. In the $^{208}\text{Pb}/^{204}\text{Pb}$ vs Pb plot, lower crust assimilation is hardly distinguishable from simple fractional crystallization (FC), as the $^{208}\text{Pb}/^{204}\text{Pb}$ ratio is weakly fractionated, resulting in flat trends (for both low- and high-Ti rocks) (Fig. 13a). However, the contamination vectors demonstrate that even minor assimilation of lower crust by the Karoo magmas will trigger significant increases in their Pb concentrations, which is not observed for either the low-Ti lava flows or most of the high-Ti rocks (except for a few lava flows).

In the $^{87}\text{Sr}/^{86}\text{Sr}$ vs Sr diagram (Fig. 13b), the model predicts a significant increase in both isotopic and elemental Sr compositions. This behavior is opposite to the trend displayed by the low-Ti group and poorly matched by the high-Ti group, regardless of whether our dataset or the literature database is considered.

In summary, qualitative observations and quantitative EC-AFC modeling based on major and trace element and isotope systematics both fail to certify significant crustal contamination of the high-Ti group, but suggest minor upper crustal contamination of the low-Ti group. These findings concur with those of Cox & Bristow (1984),

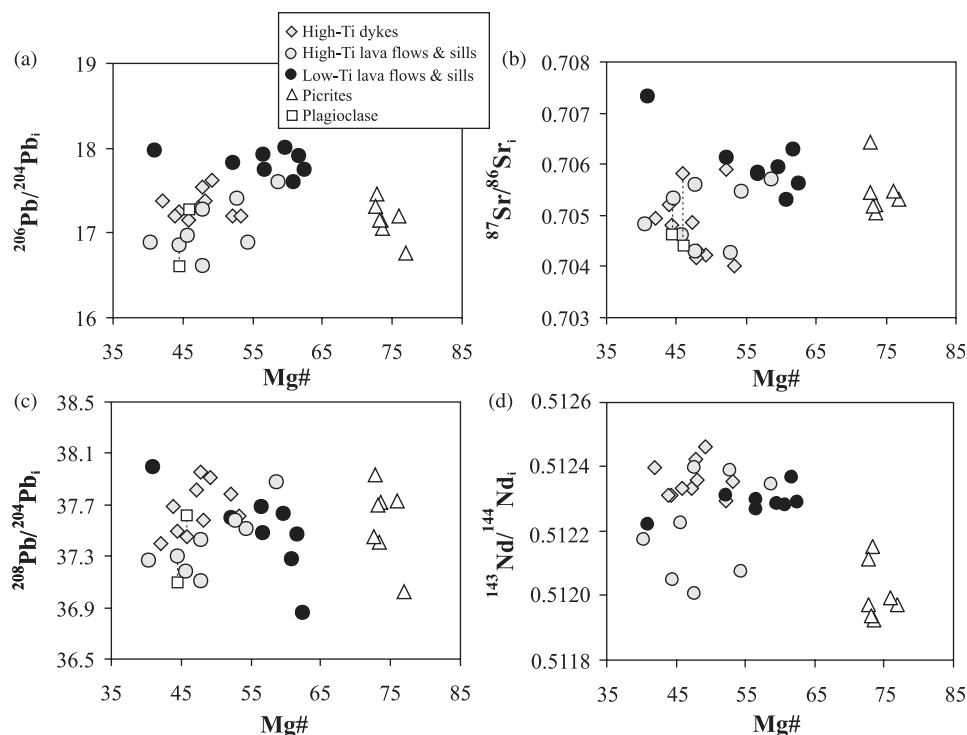


Fig. 12. $^{206}\text{Pb}/^{204}\text{Pb}$, $^{208}\text{Pb}/^{204}\text{Pb}$, $^{87}\text{Sr}/^{86}\text{Sr}$, and $^{143}\text{Nd}/^{144}\text{Nd}$ initial isotopic composition vs Mg-number. Plagioclase isotopic composition is plotted for comparison using the Mg-number of the corresponding whole-rock.

Cox (1988), and Sweeney *et al.* (1994), thus validating and extending the conclusions reached by those workers to the whole of the Karoo CFB province.

The mantle sources of the Karoo CFB

As discussed above, the $^{87}\text{Sr}/^{86}\text{Sr}$ ratios of some of the high-Ti dykes and the $^{87}\text{Sr}/^{86}\text{Sr}$ and $^{208}\text{Pb}/^{204}\text{Pb}$ ratios of some of the low-Ti lava flows and sills may have been increased by alteration and crustal assimilation processes. Except for these few isolated cases, however, we consider that, overall, the isotopic compositions of the present collection of Karoo basalts have not been modified beyond the point where they can be used as tracers of mantle source compositions.

A key point at issue concerning the origin of the Karoo CFB is whether the mantle sources involved reside within the subcontinental lithospheric mantle (SCLM; Duncan *et al.*, 1984; Hawkesworth *et al.*, 1984; Ellam & Cox, 1989; Elburg & Goldberg, 2000), are part of a mantle plume head (White & McKenzie, 1989, 1995; Campbell & Griffiths, 1990; Ernst & Buchan, 2001), or both (Cox, 1992; Ellam *et al.*, 1992; Sweeney *et al.*, 1994). In the following discussion, we present two different scenarios involving (1) heterogeneous SCLM or (2) progressive mixing between a mantle plume and the SCLM. Regardless of the scenario considered, a strong SCLM contribution is required, as will be discussed first.

Evidence for a major SCLM component

A key feature of the low- and high-Ti basalts and picrites is the LILE enrichment and the presence of negative HFSE (Nb in particular) anomalies (Fig. 5b), which contrasts with the signature of plume-related ocean island basalts (Fig. 14). These geochemical characteristics are well-established features for major CFBs (Bertrand, 1991; Arndt *et al.*, 1993; Molzahn *et al.*, 1996; Puffer, 2001; Iacumin *et al.*, 2003; Ewart *et al.*, 2004) and are generally interpreted as reflecting either (1) a mantle source composition modified by metasomatic enrichment induced by silicate melt or hydrous fluid percolation, possibly reflecting ancient subduction (Duncan *et al.*, 1984; Puffer, 2001; Ewart *et al.*, 2004), (2) asthenosphere- or plume-derived magmas interacting with lithospheric mantle (Arndt & Christensen, 1992), or (3) crustal assimilation by mantle-derived magmas (Arndt *et al.*, 1993; Taylor & McLennan, 1995). In all three cases, the negative Nb anomaly of the CFB magmas would have been inherited within the lithosphere. For the samples studied here, as discussed above, crustal contamination appears to be negligible and thus cannot account for the systematically observed negative Nb anomaly. Moreover, this anomaly is particularly pronounced in the picrites (Figs 4b and 14), which are unlikely to have undergone substantial crustal contamination (Ellam & Cox, 1989, 1991). If we therefore accept this feature to be

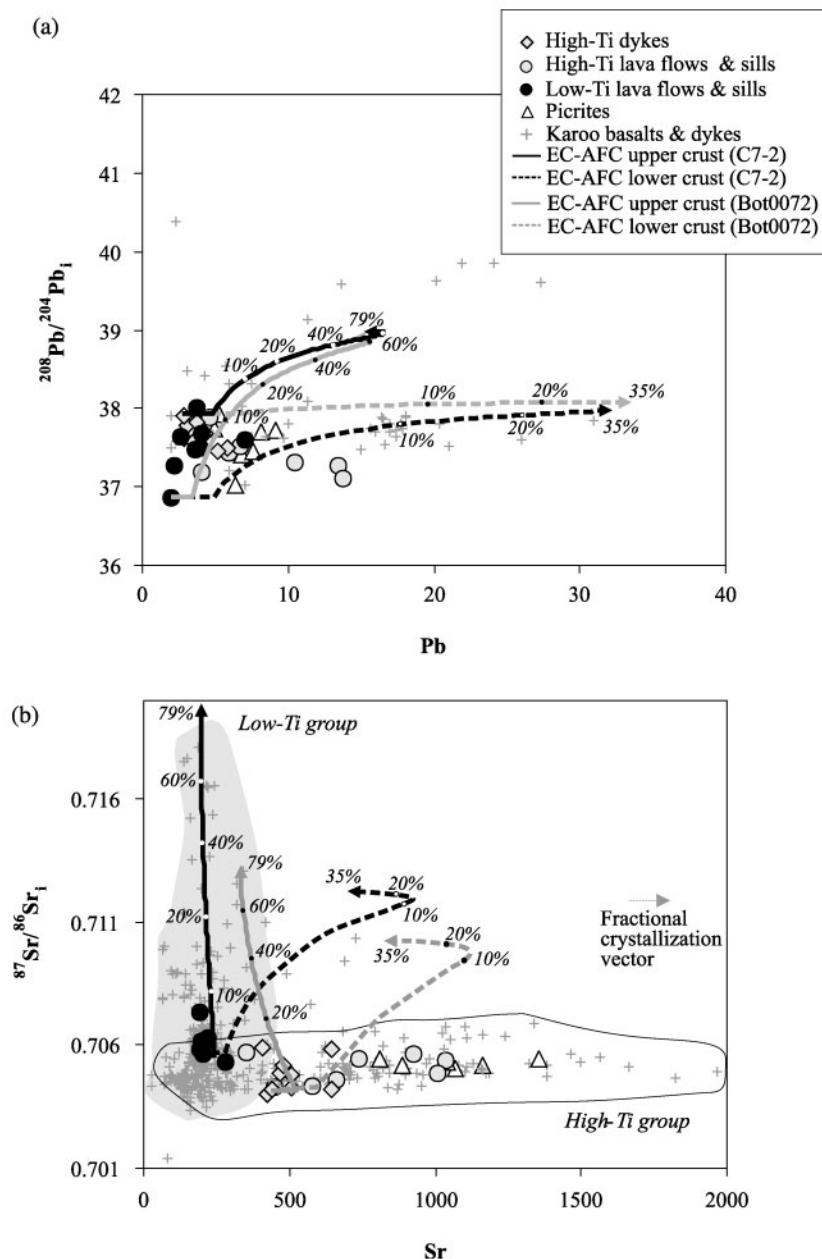


Fig. 13. Initial $^{208}\text{Pb}/^{204}\text{Pb}$ vs Pb (ppm) (a) and initial $^{87}\text{Sr}/^{86}\text{Sr}$ vs Sr (ppm) (b) with model EC-AFC curves calculated using the code of Spera & Bohron (2001). Continuous and dotted curves respectively indicate upper and lower crustal assimilation calculations with end-member compositions as given in Table 3. The calculations were run for the low-Ti (black curves) and high-Ti rocks (grey curves) using, respectively, samples C7-2 and Bot0072 as starting compositions. Small circles on curves indicate percentage of assimilated contaminant. Karoo low-Ti (grey field) and high-Ti (open field) group rocks are from the Georoc website compilation (<http://georoc.mpch-mainz.gwdg.de/georoc/>).

diagnostic of the mantle source, then an SCLM source metasomatized by (subduction-related?) silicate melts or fluids is implied. This assumption is supported by the composition of clinopyroxenes from lherzolite xenoliths sampled by kimberlites beneath the Kaapvaal craton, which display LREE enrichment and HFSE depletion (Grégoire *et al.*, 2003). The parental magma recalculated

by Grégoire *et al.* (2003) to be in equilibrium with the PIC (Phlogopite–Ilmenite–Clinopyroxene)-bearing group of xenoliths shares with Karoo basalts the features of selective LILE/HFSE fractionation, strong Nb depletion, and the absence of Zr–Hf anomalies.

Substantial melting, as would be required to produce CFBs, of the SCLM poses a problem if conditions are dry

Table 3: EC-AFC (Spera & Bohrsen, 2001) parameters for Karoo low- and high-Ti rocks and potential contaminants (lower and upper crust)

	T (°C) Upper crust	T (°C) Lower crust		Upper crust	Lower crust
Magma liquidus temperature	1200	1200	Crystallization enthalpy (J/kg)	396000	396000
Magma initial temperature	1300	1300	Isobaric specific heat of magma (J/kg per K)	1484	1484
Assimilant liquidus temperature	1000	1100	Fusion enthalpy (J/kg)	270000	350000
Assimilant initial temperature	300	600	Isobaric specific heat of assimilant (J/kg per K)	1370	1388
Solidus temperature	900	950			
Equilibration temperature	980	980			
Compositional parameters	Sr	Nd	$^{206}\text{Pb}/^{204}\text{Pb}$	$^{207}\text{Pb}/^{204}\text{Pb}$	$^{208}\text{Pb}/^{204}\text{Pb}$
<i>Botswana flood basalts, high-Ti (Bot0072)</i>					
Magma initial concentration (ppm)	440	n.u.	2.9	2.9	2.9
Magma isotope ratio	0.70421	n.u.	17.62	15.55	37.91
Magma trace element distribution coefficient	0.71	n.u.	0.17	0.17	0.17
<i>Botswana flood basalts, low-Ti (C7-2)</i>					
Magma initial concentration (ppm)	206	9.3	2.1	2.1	2.1
Magma isotope ratio	0.70563	0.512289	17.75	15.34	36.86
Magma trace element distribution coefficient	0.71	0.25	0.17	0.17	0.17
<i>Assimilant (upper crust)</i>					
Assimilant initial concentration (ppm)	159	26	18.6	18.6	18.6
Assimilant isotope ratio	0.73847	0.511800	18.83	15.89	39.19
Assimilant trace element distribution coefficient	1.5	0.25	0.56	0.56	0.56
<i>Assimilant (lower crust)</i>					
Assimilant initial concentration (ppm)	266	60.6	11.9	11.9	11.9
Assimilant isotope ratio	0.71380	0.51192	18.05	15.65	38.10
Assimilant trace element distribution coefficient	0.05	0.25	0.16	0.16	0.16

Thermodynamic parameters and Sr and Nd distribution coefficients from Bohrsen & Spera (2001). Pb distribution coefficients calculated using values reported in the GERM database (<http://earthref.org/GERM/>). High- and low-Ti basalts are represented by samples Bot0072 and C7-2, respectively. Pb and Sr elemental and isotopic compositions for upper crust inferred from strongly radiogenic Lebombo rhyolites corrected to 179 Ma (sample IR9; Betton, 1979; Betton *et al.*, 1984). Nd elemental and isotopic compositions of the upper crust after Bohrsen & Spera (2001). Lower crust composition represented by Antarctica granulites corrected at 179 Ma (Antonini *et al.*, 1999). n.u.: non-utilized.

(Arndt & Christensen, 1992), but is likely to occur if previous hydration by volatiles had taken place (Gallagher & Hawkesworth, 1992; Hawkesworth *et al.*, 1999). Turner *et al.* (1996) have calculated that an amount of 0.4% H_2O and CO_2 (Olafsson & Eggler, 1983) within the SCLM would allow the SCLM to melt enough to account for the volume of most CFBs. Although such a 'wet' mantle source is difficult to detect directly in the geochemistry of the Karoo basalts, it is corroborated by (1) the relative enrichment in LILE in these basalts, (2) the occurrence of biotite in early peridotite cumulates from the Mount Ayliff layered intrusion, which is related to the Karoo sill system (H. Bertrand, unpublished data), and (3) the occurrence of

amphibole and/or phlogopite in South African mantle xenoliths (Erlank *et al.*, 1987; Grégoire *et al.*, 2003).

The picrites and high-Ti lava flows have in common that they are the least radiogenic in Nd and Hf and the most radiogenic in ^{207}Pb and ^{208}Pb and approach the isotopic signature of some extreme alkaline magmas (Fig. 6c, e and f), such as lamproites (e.g. Leucite Hills in Montana, O'Brien *et al.*, 1995; Gaussberg in Antarctica, Murphy *et al.*, 2002; western Australia, Mitchell & Bergman, 1991) and more particularly the Karoo nephelinites (Harmer *et al.*, 1998). These alkaline rocks are commonly interpreted to have resulted from melting of metasomatic veins within the SCLM, which is supposed to first have been strongly

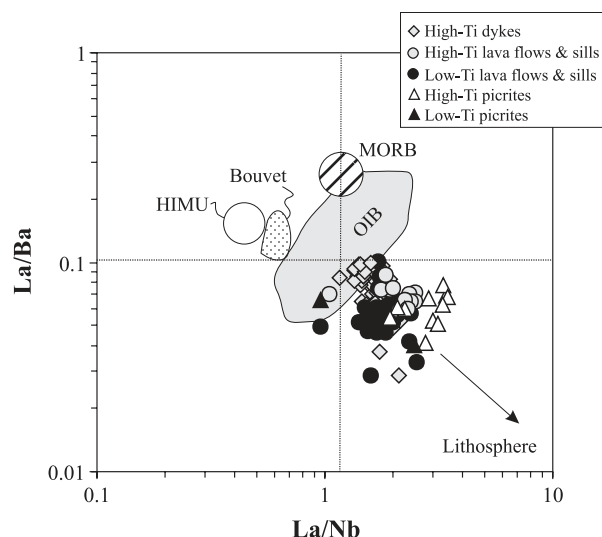


Fig. 14. La/Ba vs La/Nb with reference fields from Saunders *et al.* (1992) and Bouvet OIB field from Sun (1980). It should be noted that the Karoo rocks trend towards the inferred lithospheric mantle composition.

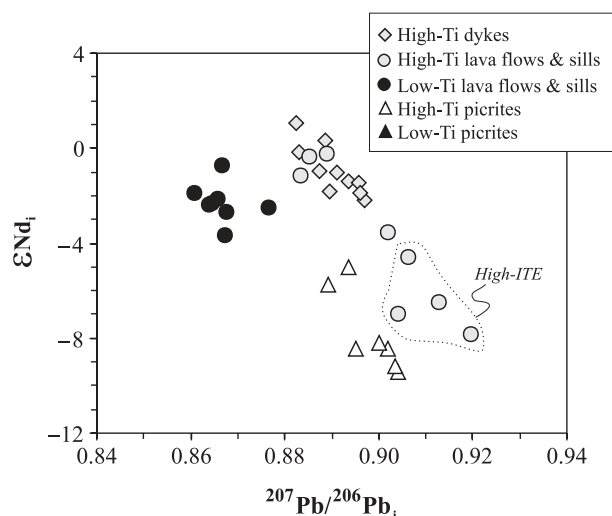


Fig. 15. Initial ϵ_{Nd} vs $^{207}\text{Pb}/^{206}\text{Pb}$. The higher $^{207}\text{Pb}/^{206}\text{Pb}$ for high-Ti compared with low-Ti basalts should be noted (see text for discussion). Dotted fields indicate the high-ITE subgroup within the high-Ti lava flows and sills groups.

enriched by subduction and metasomatic processes (Foley *et al.*, 1987; Mitchell & Bergman, 1991; Harmer *et al.*, 1998) and subsequently isolated for a long time from mantle convection (Murphy *et al.*, 2002). Similar alkaline melts have been proposed to metasomatize the SCLM beneath the Kaapvaal craton (Grégoire *et al.*, 2003).

The Pb isotopic compositions of the high-Ti rocks are characterized by low $^{206}\text{Pb}/^{204}\text{Pb}$ and relatively high $^{207}\text{Pb}/^{204}\text{Pb}$, placing them to the left of the Geochron, but above the NHRL. Therefore, as both ^{207}Pb and ^{206}Pb are the result of decay of U (^{235}U and ^{238}U , respectively),

the decoupling observed between $^{206}\text{Pb}/^{204}\text{Pb}$ and $^{207}\text{Pb}/^{204}\text{Pb}$ results from the difference between the half-lives of ^{235}U (0.7 Ga) and ^{238}U (4.5 Ga). The observed Pb isotope decoupling (hereafter $^{207}\text{Pb}/^{206}\text{Pb}$) requires at least a two-stage evolution (Murphy *et al.*, 2002, 2003) with (1) the first stage attributed to U enrichment (metasomatism?) of an initially depleted source and (2) the second stage calling for a significant amount of time spent in a low-U/Pb environment (steady-state) after U-rich partial melt extraction or addition of crustally evolved Pb from a subduction zone (e.g. Elburg & Foden, 1999). This process thus must occur in an old mantle source (Ewart *et al.*, 2004), as well as in a stable environment, two characteristics that apply to the SCLM (Hergt *et al.*, 1991). Moreover, the ϵ_{Nd} vs $^{207}\text{Pb}/^{206}\text{Pb}$ systematics of the high-Ti rocks (Fig. 15) display a strong negative correlation, indicating that their compositions depend at least partly on the age of their source (with decreasing $^{207}\text{Pb}/^{206}\text{Pb}$ with time). We suggest that the samples with the least radiogenic Nd (the nephelinite-like basalts and picrites) correspond to magmas generated from older enriched (i.e. with low Sm/Nd ratios) parts of the SCLM, whereas the more radiogenic samples (including the low-Ti basalts) were derived from younger less enriched regions.

Scenario I: Karoo mantle sources located in a heterogeneous lithospheric mantle

In this scenario, we argue that our data can be interpreted in terms of heterogeneous metasomatized SCLM and do not require chemical contribution from a mantle plume.

Heterogeneous SCLM. When the Botswana–Zimbabwe Nd–Sr isotopic data are plotted alongside those previously published (Georoc database) (Figs 6a and 16), most of the high-Ti lava flows and picrites form a well-defined trend away from BSE (Zindler & Hart, 1986), similar to that defined by some southern Africa SCLM xenoliths (Erlank *et al.*, 1987; Menzies *et al.*, 1987), towards compositions with highly negative ϵ_{Nd} (down to -22), similar to lamproites and nephelinites.

Compared with this main array, the high-Ti dykes and the low-Ti lava flows form another distinct trend departing from the same BSE-like end-member, but diverging towards enriched Sr isotope ratios. As discussed above, this second trend has been (in part) explained by alteration (the high-Ti dykes) and crustal assimilation (the low-Ti basalts) processes. Beyond the effects of these secondary processes, the samples with the least radiogenic Sr probably have source characteristics (in terms of Sr–Nd isotopes) close to those of other BSE-like high-Ti rocks. Therefore, most of the Nd–Sr isotopic range of the primary magmas (the continuous lines on Fig. 16) can be modeled by mixing between a BSE-like and a nephelinite-like component, and could reflect the degree of heterogeneity of the SCLM.

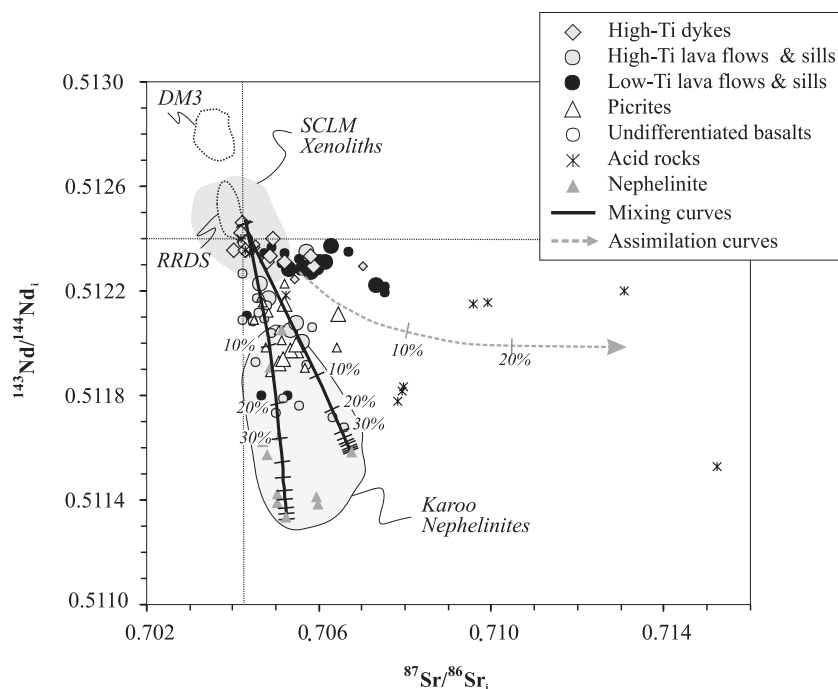


Fig. 16. Initial $^{143}\text{Nd}/^{144}\text{Nd}$ vs $^{87}\text{Sr}/^{86}\text{Sr}$. Mixing curve (continuous black line) end-members: nephelinite $^{87}\text{Sr}/^{86}\text{Sr}=0.7067$, 1034 ppm Sr; $^{143}\text{Nd}/^{144}\text{Nd}=0.51157$, 37 ppm Nd (Hawkesworth *et al.*, 1984) and ijolite $^{87}\text{Sr}/^{86}\text{Sr}=0.7052$, 633 ppm Sr; $^{143}\text{Nd}/^{144}\text{Nd}=0.51133$, 12.6 ppm Nd (Harmer *et al.*, 1998), both mixed with a SCLM xenolith composition: $^{87}\text{Sr}/^{86}\text{Sr}=0.7043$, 50 ppm Sr; $^{143}\text{Nd}/^{144}\text{Nd}=0.51244$, 2 ppm Nd (Erlank *et al.*, 1987). Dashed grey curve represents EC-AFC-calculated upper crustal assimilation of low-Ti rocks (parameters as in Table 3). Symbols as in Fig. 3, with large symbols for present study and small symbols for Karoo Georoc data recalculated to their initial values. RRDS, Rooi Rand dyke swarm (Duncan *et al.*, 1990); DM3, group 3a from Dronning Maud Land (Riley *et al.*, 2005).

In ϵNd_i – $^{206}\text{Pb}/^{204}\text{Pb}_i$ space (Fig. 6b), however, some source differences between the low- and high-Ti groups stand out. To obtain a better understanding of their origin, ϵHf and Ba/La vs Th/Yb diagrams (Fig. 17) are useful, as these variables are reliable indicators of potential sediment or fluid contributions to magma source regions (Woodhead *et al.*, 2001). Figure 17 suggests that sediments contribute to the mantle source of the high-Ti magmas, whereas the low-Ti magmas more probably originated from a source enriched by fluids.

The ϵHf_i vs ϵNd_i diagram (Fig. 6c) provides an additional means of identifying possible sediment input to the mantle source. Overall, our data define a positive correlation similar to the mantle array (slope = 1.4, J. Blichert-Toft, published and unpublished data). However, on closer inspection, the picrites differ from the rest of the samples by defining a separate trend with a substantially shallower slope (0.6) than that of the mantle array and comparable with that of the Leucite Hills lamproites (J. Blichert-Toft and B. Hanan, unpublished data). A shallower slope in ϵHf – ϵNd space indicates a mantle source with high time-integrated Lu/Hf for any given Sm/Nd, which may reflect sediments in the source (Patchett *et al.*, 1984; Blichert-Toft *et al.*, 1999; Vervoort *et al.*, 1999).

Therefore, although the low- and high-Ti magma groups exhibit similar LILE/HFSE behavior and have some isotopic features in common, they also display significant differences, which in this scenario we ascribe to derivation from a heterogeneous enriched SCLM source.

Lithosphere architecture and the distribution of low- and high-Ti magmas

Griffin *et al.* (2003) recently provided a compositional and structural map in four dimensions of the lithospheric mantle underlying the Kaapvaal craton and the surrounding mobile belts (Fig. 1), highlighting the strong vertical and lateral heterogeneity of the SCLM, from depleted harzburgites to fertile metasomatized lherzolites. One of the most striking features is a strong geochemical depletion in the depth interval between 120 and 180 km below the Limpopo belt.

Field observations show that the high-Ti rocks represent a smaller volume than the low-Ti rocks and, with the exception of minor lava flows in northern Botswana, are restricted mostly to near the Mwenzi–Tuli area and along the Shashe section of the Okavango dyke swarm (Figs 1 and 2). These rocks are located above the Limpopo–Shashe mobile belt (Fig. 1), the lateral extent of which has recently been interpreted to be greater than

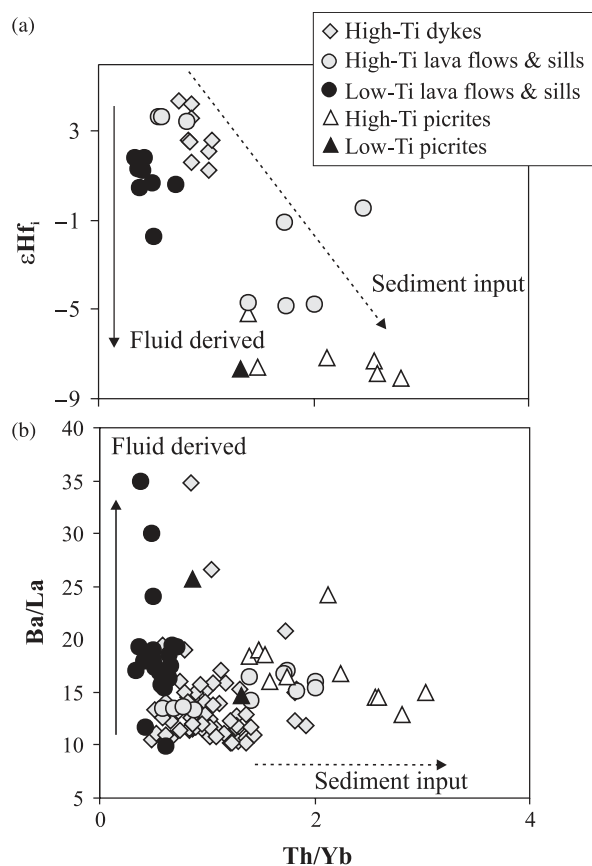


Fig. 17. (a) ϵHf_i and (b) Ba/La vs Th/Yb . Continuous vector, slab-derived fluids; dashed vector, sediment input in the source as represented and discussed by Woodhead *et al.* (2001).

previously thought (Ranganai *et al.*, 2002). This suggests that the Limpopo–Shashe mobile belt structure may have been a controlling factor in the distribution of the high-Ti magmas.

According to our calculations given above, the high-Ti magmas require garnet in their source (Fig. 9), implying a deep (>80 km) melting zone below the Limpopo–Shashe belt, as opposed to the shallow melting zone of the spinel-bearing mantle source generating the low-Ti magmas elsewhere. The depleted harzburgitic zone identified between 120 and 180 km depth below the Limpopo belt is unsuitable for producing significant amounts of melting. However, at depths greater than 200 km, the presence of strongly metasomatized peridotites has been documented (Griffin *et al.* 2003); these represent a relatively fertile zone for magma supply at the garnet-bearing base of the SCLM, which is about 200–300 km thick (James *et al.*, 2001).

As an example, in the $^{143}\text{Nd}/^{144}\text{Nd}_i$ vs $^{87}\text{Sr}/^{86}\text{Sr}_i$ diagram (Fig. 16), the trend between the high-Ti picrites, enriched in Nd–Hf isotope space, and the BSE-like mantle source may be interpreted as follows: (1) the highly enriched picritic (and some basaltic high-Ti) magmas could reflect the

contribution of deep vein-like material percolating through the base of the SCLM, possibly reflecting sediment input (Fig. 17); (2) the BSE-like mantle is more likely to represent the SCLM itself, playing the role of matrix to the veins and enriched by fluid-related processes (Fig. 17); (3) as the depth of melting decreases and the degree of melting increases (illustrated, respectively, by the decrease of the $(\text{Sm/Yb})_n$ and $(\text{La/Yb})_n$ ratios; Fig. 18), the veined material vanishes and the BSE-like mantle signature becomes predominant.

The increasing degree of melting from deeper to shallower SCLM derived from our modeling (Fig. 9) may appear counterintuitive in the case of a homogeneous lithospheric mantle, for which one would expect larger degrees of melting near the base of the SCLM (where most of the heat is accumulated). However, this apparent contradiction can be accommodated by a strong vertical (and lateral) heterogeneity of the SCLM (Griffin *et al.*, 2003), as the shallower SCLM generally consists of fertile lherzolite (especially in north and south Botswana), whereas the deepest SCLM (especially beneath the Limpopo belt) consists of depleted or melt-metasomatized re-enriched peridotites (more difficult to melt?).

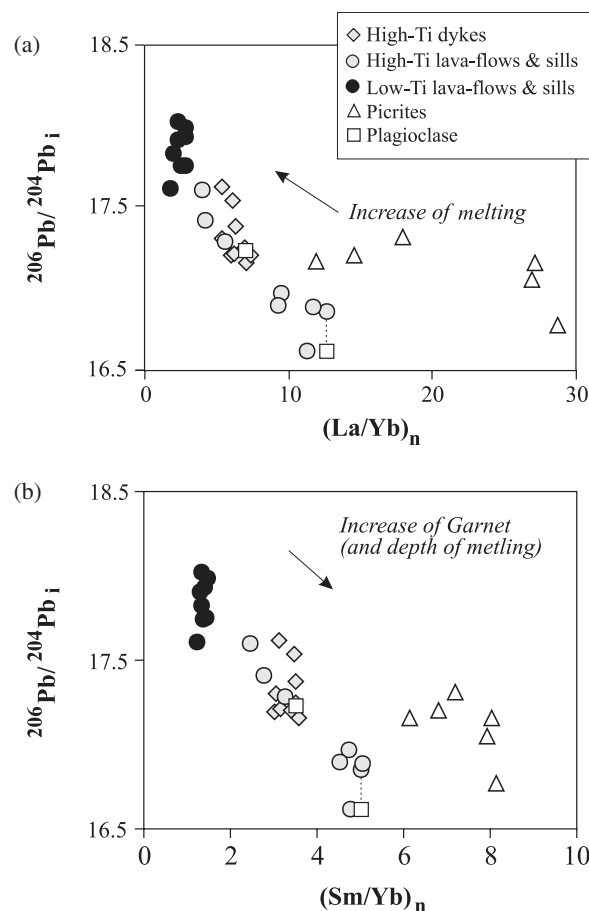


Fig. 18. Initial $^{206}\text{Pb}/^{204}\text{Pb}$ as a function of $(\text{La}/\text{Yb})_n$ (a) and $(\text{Sm}/\text{Yb})_n$ (b). Schematic vectors (according to Fig. 9) show in (a) increase in degree of source melting and in (b) increase in the amount of garnet in the source, which in turn indicates increasing depth of melting (see text for discussion).

In this scenario, we emphasize the importance of the strong vertical and horizontal heterogeneity of the SCLM, consistent with the general picture inferred from mantle xenoliths (Griffin *et al.*, 2003), which is key to producing the Karoo magmas through polybaric melting. This scenario does not exclude a mantle plume as the supplier of the necessary thermal energy, although thermal insulation beneath a mega-continent as a shield effect (e.g. Anderson *et al.*, 1992; Coltice *et al.*, 2007) is also feasible.

Scenario II: mixing between lithospheric and sub-lithospheric mantle (plume)

A sub-lithospheric mantle plume component. In the previous section, the Karoo nephelinites and picrites were shown to be likely to represent an SCLM-enriched end-member. In our second scenario, we now envisage an additional sub-lithospheric component with slightly depleted isotopic compositions. The sub-lithospheric component may be portrayed by either (1) an OIB-like mantle plume that possibly originated at the core–mantle or lower–upper

mantle boundaries (e.g. Riley *et al.*, 2003) or (2) a relatively depleted asthenospheric mantle (Ellam, 2006). By definition, these potential components would have Sr–Nd (and Hf) isotopic compositions between those of BSE and isotopically depleted OIB (Fig. 6). Because of the chemical contrast between this component and the extremely ITE-enriched veined SCLM, mixing between these two end-members would be strongly affected (and masked) by the SCLM signature and would readily result in negative ϵNd_i and ϵHf_i and relatively unradiogenic Pb and Sr isotopic compositions (e.g. Ellam, 2006).

The rocks with the compositions closest to this sub-lithospheric component are the high-Ti Okavango dykes and the low-Ti basalts. These rocks do not overlap with either the Discovery, Bouvet, or Shona OIB or MORB isotopic compositions (Figs 6 and 14), but, as mentioned above, this can be explained by substantial contamination by the SCLM (as monitored by the minor negative Nb anomaly) and/or upper crustal contamination in the case of the low-Ti basalts. A gradually increasing contribution from a mantle plume component as the Sr and Nd isotopic

compositions of the Karoo rocks approach BSE (Fig. 16) also is in accordance with the observed decrease of the size of the negative Nb anomaly (from the picrites to the high-Ti dykes). The low-Ti basalts may represent the most 'plume-like' end-member of the southern Africa Karoo suite (e.g. Fig. 6f), but, as shown above, the low-Ti rocks are likely to have suffered from various degrees of upper crustal contamination and therefore are not reliable samples for testing this hypothesis. According to calculations carried out on Karoo-equivalent rocks from Dronning Maud Land by Riley *et al.* (2005), mixing between an isotopically depleted (plume?) end-member (group DM3a; Fig. 16) and 3% of a partial melt of an enriched SCLM can reproduce the Sr and Nd isotopic compositions of the Okavango dykes, although the composition of the depleted plume itself is not well constrained.

Mixing between the SCLM and a mantle plume component. As in the first scenario, the increasing melt fraction with time and the degree of melting occurring at progressively shallower levels are illustrated by, respectively, the La/Yb and Sm/Yb ratios (and the modal peridotitic garnet and spinel contents derived from these ratios; Figs 9 and 18). The temporal order of eruption of the different magma types is constrained by the stratigraphy of the various Karoo formations as observed in the field (e.g. Eales *et al.*, 1984).

In this scenario, the Karoo magmatism is hypothesized to have started by the arrival of a sub-lithospheric mantle plume impacting at the base of the SCLM near the Mwenezi area. The plume provided sufficient heat to melt the alkaline veins (compare with the discussion for scenario 1) at the base of the lithospheric mantle beneath the Limpopo belt (in the garnet-bearing lherzolite facies) and gave rise to the Karoo nephelinites by low degrees of melting. The subsequent progressive ascent of the mantle plume allowed the melting of both the SCLM and the mantle plume. This process generated first the high-Ti (low degrees of melting) and then the low-Ti (slightly higher degrees of melting) picrites. Because of the progressive thermal and mechanical erosion of the SCLM (e.g. Olson, 1988) and/or the lithospheric extension as a result of continuing rifting, the plume continued to rise and expand and contributed increasingly to the magma production. The resulting mixtures are reflected in the magmatic evolution from high-Ti/high-ITE basalts over high-Ti basaltic dykes to high-Ti/low-ITE basalts as the plume kept ascending. An increasing contribution of the mantle plume with decreasing influence of the SCLM is also suggested by the diminution of the negative Nb anomaly.

The entire stratigraphic succession as described above is restricted to only the Mwenezi–Limpopo belt area. As shown previously in scenario 1, the lithosphere beneath the Limpopo belt is likely to be thicker and chemically

more enriched at the base (James *et al.*, 2001; Griffin *et al.*, 2003), the chemically enriched component being best visualized as alkaline veins. A larger thickness of the lithosphere would have prevented full mechanical–thermal erosion of the SCLM and thus more complete decompression melting of the mantle plume. However, as mentioned above, the southern African lithosphere is strongly heterogeneous and likely to be thinner and vein-free in the cratonic areas surrounding the Limpopo belt. The cratonic lithosphere therefore allows for faster and easier upwelling of a mantle plume up to the level of the spinel-bearing lherzolite facies, thereby preventing significant contamination of the magmas by the SCLM. Ultimately, the mantle plume generated the low-Ti basalts over a large area in southern Africa (Fig. 1) by high degrees of decompression melting. The low-Ti magmas seem to have experienced a fairly small contribution from the melting of the SCLM veins, but instead were moderately affected by upper crustal contamination, perhaps as a result of longer residence time in the upper crust and/or their BSE-to-depleted compositions.

In this scenario, we therefore propose two end-members represented by (1) the metasomatically enriched alkaline veins of the SCLM and (2) a sub-lithospheric (asthenospheric- or OIB-like?) mantle plume. We suggest that our data are consistent with a progressive increase of a mantle plume contribution as the plume rises and expands through a laterally and vertically heterogeneous lithosphere. We note that this scenario is, to some extent, similar to the scenarios proposed for the North Atlantic Tertiary Province (Kerr, 1994) and the Mesoproterozoic Zig-Zag Dal basalts (Upton *et al.*, 2005), although in the case of Karoo, the lithosphere exerts a strong control on the magma distribution and composition.

CONCLUSIONS

Our new geochemical and Sr, Nd, Hf, and Pb isotopic data on basaltic and picritic lava flows and dykes and basaltic sills from the southern Zimbabwe and Botswana magmatic province provide information on the petrogenesis and mantle source origins of the Karoo large igneous province.

Two subgroups have been identified (the low- and high-Ti groups). They share LILE/HFSE enrichment with a marked negative Nb anomaly, but display contrasting ITE and REE fractionation and isotopic compositions. Contrasting MREE/HREE ratios are explained by the different modal compositions of their sources. Calculations show that the low-Ti magmas were derived from the melting of a spinel-bearing (2%) lherzolite, whereas the high-Ti magmas require the presence of, respectively, 2%, 2–4%, and 4–7% garnet in the source of the basaltic dykes, basaltic lava flows, and picrites, suggesting a deeper-seated origin compared with the low-Ti source. The melting

process is accompanied at shallower levels by up to 50% fractional crystallization of gabbroic assemblages for both groups and by minor upper crustal contamination of the low-Ti rocks.

The isotopic variations and LREE/HFSE fractionation of both low- and high-Ti magmas suggest the dominance of a sub-continental lithospheric mantle (SCLM) component in the Karoo magmatism. The Karoo magmatic sequence can be explained equally well by two contrasting scenarios between which the present data cannot distinguish unambiguously. In the first, the magmas are derived from a heterogeneous SCLM, metasomatically enriched in the form of veins (sediment input?) during ancient subduction events. The Karoo magmas document polybaric melting from a deeper 'nephelinite-veined' source (the most ITE-enriched basaltic lava flows and picrites) to a shallower BSE-like (high-Ti dykes, low-Ti and the least ITE-enriched high-Ti lava flows) SCLM. In the second scenario, the different magma types reflect mixing between the veined SCLM proposed in the first scenario and a (OIB- or asthenospheric-like?) mantle plume. The contribution of the mantle plume to the Karoo magmas is minimal for the nephelinites and increases progressively as the plume rises and expands through a laterally and vertically heterogeneous lithosphere (i.e. increases from high-Ti picrites to low-Ti basalts).

The distribution of the high- and low-Ti magmas reflects strong control by the lithospheric architecture. The high-Ti magmas are restricted to areas above the thick Limpopo belt lithosphere, whereas the low-Ti magmas are located on the thinner (and vein-free) Kaapvaal and Zimbabwe cratonic lithospheres. The occurrence of a low- ϵNd_i , low- ϵHf_i , and low- $^{206}\text{Pb}/^{204}\text{Pb}_i$ mantle source (thick veined SCLM?) is possibly due to higher degrees of subduction-related metasomatism (and sediment input?) beneath the Limpopo belt.

ACKNOWLEDGEMENTS

We dedicate this paper to the memory of our friend Henri Kampunzu, who passed away in November 2004. B. Le Gall, G. Tshoso, J. J. Tiercelin, and M. Watkeys are thanked for their help in the field. We are grateful to P. Capiez for XRF analyses and to P. Télouk for help with the MC-ICP-MS. We also thank C. Tonani, Head of the Cultural and Scientific Service of the French Embassy in Botswana, for his support in developing and carrying out this program. The Lobatse Geological Survey of Botswana is acknowledged for allowing us to sample the boreholes. Finally, we thank R. Elam, T. Riley, and M. Elburg for helpful reviews of our manuscript. This work is part of a collaboration between the Universities of Nice, Lyon, and Brest in France and the Universities of Botswana and Kwazulu-Natal in South Africa and was supported

financially through the CNRS-INSU program 'Interieur de la Terre'.

SUPPLEMENTARY DATA

Supplementary data for this paper are available at *Journal of Petrology* online.

REFERENCES

- Albarède, F., Luais, B., Fitton, G., Semet, M., Kaminski, E., Upton, B. G. J., Bachèlery, P. & Cheminée, J.-L. (1997). The geochemical regimes of Piton de la Fournaise volcano (Réunion) during the last 530 000 years. *Journal of Petrology* **38**, 171–201.
- Allègre, C. J., Lewin, E. & Dupre, B. (1988). A coherent crust–mantle model for the uranium–thorium–lead isotopic system. *Chemical Geology* **70**, 211–234.
- Anderson, D. L. (1994). The sub-lithospheric mantle as the source of continental flood basalts; the case against the continental lithosphere and plume head reservoirs. *Earth and Planetary Science Letters* **123**, 269–280.
- Anderson, D. L., Zhang, Y. S. & Tanimoto, T. (1992). Plume heads, continental lithosphere, flood basalts and tomography. In: Alabaster, T., Storey, B. C. & Pankhurst, R. J. (eds) *Magmatism and the Causes of Continental Break-up*. Geological Society, London, *Special Publications* **68**, 99–124.
- Antonini, P., Piccirillo, E. M., Petrini, R., Civetta, L., D'Antonio, M. & Orsi, G. (1999). Enriched mantle–Dupal signature in the genesis of the Jurassic Ferrar tholeiites from Prince Albert Mountains (Victoria Land, Antarctica). *Contributions to Mineralogy and Petrology* **136**, 1–19.
- Arndt, N. & Christensen, U. (1992). The role of lithospheric mantle in continental flood volcanism; thermal and geochemical constraints. *Journal of Geophysical Research* **97**, 10967–10981.
- Arndt, N. T., Czamanske, G. K., Wooden, J. L. & Fedorenko, V. A. (1993). Mantle and crustal contributions to continental flood volcanism. *Tectonophysics* **223**, 39–52.
- Bertrand, H. (1991). The Mesozoic tholeiitic province of Northwest Africa: a volcano-tectonic record of the early opening of Central Atlantic. In: Kampunzu, A. B. & Lubala, R. T. (eds) *Magmatism in extensional structural settings*. Berlin: Springer, pp. 147–188.
- Betton, P. J. (1979). Isotopic evidence for crustal contamination in the Karoo rhyolites of Swaziland. *Earth and Planetary Science Letters* **45**, 263–274.
- Betton, P. J., Armstrong, R. A. & Manton, W. I. (1984). Variations in the lead isotopic composition of the Karoo magmas. In: Erlank, A. J. (ed.) *Petrogenesis of the Volcanic Rocks of the Karoo Province*. Special Publication of the Geological Society of South Africa **13**, 331–339.
- Blichert-Toft, J. (2001). On the Lu–Hf isotope geochemistry of chondrites and the evolution of the mantle–crust system. *Geostandards Newsletter* **25**, 41–56.
- Blichert-Toft, J., Chauvel, C. & Albarède, F. (1997). Separation of Hf and Lu for high-precision isotope analysis of rock samples by magnetic sector multiple collector ICP-MS. *Contributions to Mineralogy and Petrology* **127**, 248–260.
- Blichert-Toft, J., Chauvel, C. & Albarède, F. (1999). Hf isotopes evidence for pelagic sediments in the source of Hawaiian basalts. *Science* **285**, 879–882.
- Blichert-Toft, J., Agranier, A., Andres, M., Kingsley, R., Schilling, J.-G. & Albarède, F. (2005). Geochemical segmentation of the Mid-Atlantic Ridge north of Iceland and ridge-hot spot

- interaction in the North Atlantic. *Geochemistry, Geophysics, Geosystems* **6**, Q01E19, doi:10.1029/2004GC000788.
- Bohrson, W. A. & Spera, F. (2001). Energy-constrained open-system magmatic processes II: Application of energy constrained assimilation–fractional crystallization (EC-AFC) model to magmatic systems. *Journal of Petrology* **42**, 1019–1041.
- Boynton, W. V. (1984). Geochemistry of the rare earth elements: meteorite studies. In: Henderson, P. (ed.) *Rare Earth Element Geochemistry*. Amsterdam: Elsevier, pp. 63–114.
- Brewer, T. S., Rex, D., Guise, P. G. & Hawkesworth, C. J. (1996). Geochronology of Mesozoic tholeiitic magmatism in Antarctica: implications for the development of the failed Weddell Sea rift system. In: Storey, B. C., King, E. C. & Livermore, R. A. (eds) *Weddell Sea Tectonics and Gondwana Break-up*. Geological Society, London, *Special Publications* **108**, 45–61.
- Bristow, J. W., Allsopp, H. L., Erlank, A. J., Marsh, J. S. & Armstrong, R. A. (1984). Strontium isotope characterization of Karoo volcanic rocks. In: Erlank, A. J. (ed.) *Petrogenesis of the Volcanic Rocks of the Karoo Province*. Special Publication of the Geological Society of South Africa **13**, 295–329.
- Burke, K. & Dewey, J. F. (1972). Plume generated triple junctions. Key indicators in applying plate tectonics to old rocks. *Journal of Geology* **81**, 403–433.
- Campbell, I. H. & Griffiths, R. W. (1990). Implications of mantle plume structure for the evolution of flood basalts. *Earth and Planetary Science Letters* **99**, 79–73.
- Carney, J. N., Aldiss, D. T. & Lock, N. P. (1994). The geology of Botswana. *Botswana Geological Survey Bulletin* **17**, 113 pp.
- Chavez Gomez, S. (2001). *A Catalogue of Dykes from Aeromagnetic Surveys in Eastern and Southern Africa* ITC Publication **80**.
- Coltice, N., Phillips, B. R., Bertrand, H., Ricard, Y. & Rey, P. (2007). Global warming of the mantle at the origin of flood basalts over supercontinents. *Geology* (in press).
- Courtillot, V. E. & Renne, P. R. (2003). On the ages of flood basalt events. *Comptes Rendus Geosciences* **335**, 113–140.
- Courtillot, V., Jaupart, C., Manighetti, I., Tapponnier, P. & Besse, J. (1999). On causal links between flood basalts and continental breakup. *Earth and Planetary Science Letters* **166**, 177–195.
- Cox, K. G. (1988). The Karoo Province. In: MacDougall, J. D. (ed.) *Continental Flood Basalts*. Dordrecht: Kluwer, pp. 239–271.
- Cox, K. G. (1992). Karoo igneous activity, and the early stages of the break-up of Gondwanaland. In: Storey, B. C., Alabaster, T. & Pankhurst, R. J. (eds) *Magmatism and the Causes of Continental Break-up*, Special Publication of the Geological Society of London **13**, pp. 137–148.
- Cox, K. G. & Bristow, J. W. (1984). The Sabie River basalt formation of the Lebombo monocline and south-east Zimbabwe. *Transactions of the Geological Society of South Africa, Special Publication* **13**, 125–147.
- Cox, K. G., Johnson, R. L., Monkman, L. J., Stillman, C. J., Vail, J. R. & Wood, D. N. (1965). The geology of the Nuanetsi Igneous Province. *Philosophical Transactions of the Royal Society of London, Series A* **257**, 71–218.
- Cox, K. G., Macdonald, R. & Hornung, G. (1967). Geochemical and petrographical provinces in the Karoo basalts of southern Africa. *American Mineralogist* **52**, 1451–1474.
- Douglass, J., Schilling, J. G. & Fontignie, D. (1999). Plume–ridge interactions of the Discovery and Shona with the southern Mid-Atlantic Ridge (45°–55°S). *Journal of Geophysical Research* **104**, 2941–2962.
- Duncan, A. R., Erlank, A. J. & Marsh, J. S. (1984). Regional geochemistry of the Karoo igneous province. In: Erlank, A. J. (ed.) *Petrogenesis of the Volcanic Rocks of the Karoo Province*. Special Publication of the Geological Society of South Africa **13**, 355–388.
- Duncan, A. R., Armstrong, R. A., Erlank, A. J., Marsh, J. S. & Watkins, R. T. (1990). MORB-related dolerites associated with the final phases of Karoo flood basalt volcanism in southern Africa. In: Parker, A. J., Rickwood, P. C. & Tucker, D. H. (eds) *Mafic Dykes and Emplacement Mechanisms*. Rotterdam: Balkema, pp. 119–129.
- Duncan, A. R., Hooper, P. R., Rehacek, J., Marsh, J. S. & Duncan, A. R. (1997). The timing and duration of the Karoo igneous event, southern Gondwana. *Journal of Geophysical Research* **102**, 18127–18138.
- Eales, H. V., Marsh, J. S. & Cox, K. G. (1984). The Karoo igneous province: an introduction. In: Erlank, A. J. (ed.) *Petrogenesis of the Volcanic Rocks of the Karoo Province*. Special Publication of the Geological Society of South Africa **13**, 1–26.
- Elburg, M. & Foden, J. (1999). Sources for magmatism in central Sulawesi; geochemical and Sr–Nd–Pb isotopic constraints. *Chemical Geology* **156**, 67–93.
- Elburg, M. & Goldberg, A. (2000). Age and geochemistry of Karoo dolerite dykes from northeast Botswana. *Journal of African Earth Sciences* **31**, 539–554.
- Ellam, R. M. (2006). New constraints on the petrogenesis of the Nuanetsi picrite basalts from Pb and Hf isotope data. *Earth and Planetary Science Letters* **245**, 153–161.
- Ellam, R. M. & Cox, K. G. (1989). A Proterozoic lithospheric source for Karoo magmatism: evidence from the Nuanetsi picrites. *Earth and Planetary Science Letters* **92**, 207–218.
- Ellam, R. M. & Cox, K. G. (1991). An interpretation of Karoo picrite basalts in terms of interaction between asthenospheric magmas and the mantle lithosphere. *Earth and Planetary Science Letters* **105**, 330–342.
- Ellam, R. M., Carlson, R. W. & Shirley, S. B. (1992). Evidence from Re–Os isotopes for plume–lithosphere mixing in Karoo flood basalt genesis. *Nature* **359**, 718–721.
- Encarnacion J., Fleming, T. H., Elliot, H., Eales, H. V. (1996). Synchronous emplacement of Ferrar and Karoo dolerites and the early breakup of Gondwana. *Geology* **24**, 535–538.
- Erlank, A. J., Hawkesworth, C. J., Haggerty, S. E., Allsopp, H. L., Rickard, R. S. & Menzies, M. A. (1987). Evidence for mantle metasomatism in peridotite nodules of the Kimberley pipes, South Africa. In: Hawkesworth, C. J. & Menzies, M. (eds) *Mantle Metasomatism*. New York: Academic Press, pp. 221–331.
- Ernst, R. E. & Buchan, K. L. (2001). Large mafic magmatic events through time and links to mantle-plume heads. In: Ernst, R. E. & Buchan, K. L. (eds) *Mantle Plumes: their Identification Through Time*. Geological Society of America, *Special Papers* **352**, 483–566.
- Ewart, A., Marsh, J. S., Milner, S. C., Duncan, A. R., Kamber, B. S. & Armstrong, R. A. (2004). Petrology and geochemistry of Early Cretaceous bimodal continental flood volcanism of the NW Etendeka, Namibia. Part 1: Introduction, mafic lavas and re-evaluation of mantle source components. *Journal of Petrology* **45**, 59–105.
- Foley, S. F., Venturelli, G., Green, D. H. & Toscani, L. (1987). The ultrapotassic rocks; characteristics, classification, and constraints for petrogenetic models. *Earth-Science Reviews* **24**, 81–134.
- Gallagher, K. & Hawkesworth, C. (1992). Dehydration melting and the generation of continental flood basalts. *Nature* **358**, 57–59.
- Ghiorso, M. S. & Sack, R. O. (1995). Chemical transfer in magmatic processes IV. A revised and internally consistent thermodynamic model for the interpolation and extrapolation of liquid–solid equilibria in magmatic systems at elevated temperatures and pressures. *Contributions to Mineralogy and Petrology* **119**, 197–212.
- Grégoire, M., Bell, D. R. & Le Roex, A. P. (2003). Garnet lherzolites from the Kaapvaal Craton (South Africa): trace element evidence for a metasomatic history. *Journal of Petrology* **44**, 629–657.

- Griffin, W. L., O'Reilly, S. Y., Natapov, L. M. & Ryan, C. G. (2003). The evolution of lithospheric mantle beneath the Kalahari Craton and its margins. *Lithos* **71**, 215–241.
- Harmer, R. E., Lee, C. A. & Eglington, B. M. (1998). A deep mantle source for carbonatite magmatism: evidence from the nephelinites and carbonatites of the Buhera district, SE Zimbabwe. *Earth and Planetary Science Letters* **158**, 131–142.
- Harris, C. & Erlank, A. J. (1992). The production of large-volume, low- $\delta^{18}\text{O}$ rhyolites during the rifting of Africa and Antarctica: the Lebombo monocline, southern Africa. *Geochimica et Cosmochimica Acta* **56**, 3561–3570.
- Hart, S. R. (1984). A large-scale isotope anomaly in the southern hemisphere mantle. *Nature* **309**, 753–757.
- Hawkesworth, C. J., Marsh, J. S., Duncan, A. R., Erlank, A. J. & Norry, M. J. (1984). The role of continental lithosphere in the generation of the Karoo volcanic rocks: evidence from combined Nd- and Sr-isotope studies. In: Erlank, A. J. (ed.) *Petrogenesis of the Volcanic Rocks of the Karoo Province. Special Publication of the Geological Society of South Africa* **13**, 341–354.
- Hawkesworth, C., Kelley, S., Turner, S., Le Roex, A. & Storey, B. (1999). Mantle processes during Gondwana break-up and dispersal. *Journal of African Earth Sciences* **28**, 239–261.
- Hergt, J. M., Peate, D. W. & Hawkesworth, C. J. (1991). The petrogenesis of Mesozoic Gondwana low-Ti flood basalts. *Earth and Planetary Science Letters* **105**, 134–148.
- Hill, R. I. (1991). Starting plume and continental break-up. *Earth and Planetary Science Letters* **104**, 398–416.
- Iacumin, M., De Min, A., Piccirillo, E. M. & Bellieni, G. (2003). Source mantle heterogeneity and its role in the genesis of Late Archaean–Proterozoic (2.7–1.0 Ga) and Mesozoic (200 and 130 Ma) tholeiitic magmatism in the South American Platform. *Earth-Science Reviews* **62**, 365–397.
- James, D. E., Fouch, M. J., VanDecar, J. C., Van Der Lee, S. & Kaapvaal Seismic Group (2001). Tectospheric structure beneath southern Africa. *Geophysical Research Letters* **28**, 2485–2488.
- Jones, D. L., Duncan, R. A., Briden, J. C., Randall, D. E. & MacNiocaill, C. (2001). Age of the Batoka basalts, northern Zimbabwe, and the duration of Karoo Large Igneous Province magmatism. *Geochemistry, Geophysics, Geosystems* **2**, paper number 2000GC000110.
- Jourdan, F., Féraud, G., Bertrand, H., Kampunzu, A. B., Tshoso, G., Le Gall, B., Tiercelin, J. J. & Capiez, P. (2004). The Karoo triple junction questioned: evidence from $^{40}\text{Ar}/^{39}\text{Ar}$ Jurassic and Proterozoic ages and geochemistry of the Okavango dyke swarm (Botswana). *Earth and Planetary Science Letters* **222**, 989–1006.
- Jourdan, F., Féraud, G., Bertrand, H., Kampunzu, A. B., Tshoso, G., Watkeys, M. K. & Le Gall, B. (2005). The Karoo large igneous province: brevity, origin, and relation with mass extinction questioned by new $^{40}\text{Ar}/^{39}\text{Ar}$ age data. *Geology* **33**, 745–748.
- Jourdan, F., Féraud, G., Bertrand, H., Watkeys, M. K., Kampunzu, A. B. & Le Gall, B. (2006). Basement control on dyke distribution in Large Igneous Provinces: case study of the Karoo triple junction. *Earth and Planetary Science Letters* **241**, 307–322.
- Jourdan, F., Féraud, G., Bertrand, H. & Watkeys, M. K. (2007). From flood basalts to the onset of oceanisation: example from the $^{40}\text{Ar}/^{39}\text{Ar}$ high-resolution picture of the Karoo large igneous province. *Geochemistry, Geophysics, Geosystems* **8**, Q02002.
- Jourdan, F., Féraud, G., Bertrand, H., Watkeys, M.K., Renne, P.R. Distinct brief major events in the Karoo large igneous province clarified by new $^{40}\text{Ar}/^{39}\text{Ar}$ ages on the Lesotho basalts. *Lithos*, (in press).
- Key, R. M. & Ayres, N. (2000). The 1998 edition of the National Geological Map of Botswana. *Journal of African Earth Sciences* **30**, 427–451.
- Le Bas, M. J., Le Maitre, R. W., Streickeisen, A. & Zanettin, B. (1986). A chemical classification of volcanic rocks based on the total alkali–silica diagram. *Journal of Petrology* **27**, 745–750.
- Le Gall, B., Tshoso, G., Jourdan, F., Féraud, G., Bertrand, H., Tiercelin, J. J., Kampunzu, A. B., Modisi, M. P., Dymant, J. & Maya, J. (2002). $^{40}\text{Ar}/^{39}\text{Ar}$ geochronology and structural data from the giant Okavango and related mafic dyke swarms, Karoo igneous province, Botswana. *Earth and Planetary Science Letters* **202**, 595–606.
- Le Gall, B., Tshoso, G., Dymant, J., Kampunzu, A. B., Jourdan, F., Féraud, G., Bertrand, H. & Aubourg, C. (2005). The Okavango giant mafic dyke swarm (NE Botswana) and its structural significance within the Karoo Large Igneous Province. *Journal of Structural Geology* **27**, 2234–2255.
- Luttinen, A. V. & Furnes, H. (2000). Flood basalts of Vestfjella: Jurassic magmatism across an Archaean–Proterozoic lithospheric boundary in Dronning Maud Land, Antarctica. *Journal of Petrology* **41**, 1271–1305.
- Manhès, G., Minster, J. F. & Allègre, C. J. (1978). Comparative U–Th–Pb and Rb–Sr study of the Saint Séverin amphoterite: consequence for early solar system chronology. *Earth and Planetary Science Letters* **39**, 14–24.
- Marsh, J. S., Hooper, P. R., Rehacek, J., Duncan, R. A. & Duncan, A. R. (1997). Stratigraphy and age of Karoo basalts of Lesotho and implications for correlation within the Karoo igneous province. In: Mahoney, J. J. & Coffin, M. F. (eds) *Large Igneous Provinces: Continental, Oceanic and Planetary Flood Volcanism. Geophysical Monograph, American Geophysical Union* **100**, 247–272.
- Marsh, J. S. (2002). Discussion “The geophysical mapping of Mesozoic dyke swarms in southern Africa and their origin in the disruption of Gondwana”, *Journal of African Earth Sciences* **35**, 525–527.
- McKenzie, D. & O’Nions, R. K. (1991). Partial melt distribution from inversion of rare earth element concentrations. *Journal of Petrology* **32**, 1021–1091.
- Menzies, M. A., Rogers, N., Tindle, A. & Hawkesworth, C. J. (1987). Metasomatic and enrichment processes in lithospheric peridotites, an effect of asthenosphere–lithosphere interaction. In: Menzies, M. A. & Hawkesworth, C. J. (eds) *Mantle Metasomatism*. London: Academic Press, pp. 313–361.
- Mitchell, R. H. & Bergman, S. C. (1991). *Petrology of Lamproites*. New York: Plenum.
- Molzahn, M., Reisberg, L. & Wörner, G. (1996). Os, Sr, Nd, Pb, O isotope and trace element data from the Ferrar flood basalts, Antarctica: evidence for an enriched subcontinental lithospheric source. *Earth and Planetary Science Letters* **144**, 529–545.
- Murphy, D. T., Collerson, K. D. & Kamber, B. S. (2002). Lamproites from Gaussberg, Antarctica: possible transition zone melts of Archaean subducted sediments. *Journal of Petrology* **43**, 981–1001.
- Murphy, D. T., Kambers, B. S. & Collerson, K. D. (2003). A refined solution to the first terrestrial Pb-isotope paradox. *Journal of Petrology* **44**, 39–53.
- O’Brien, H. E., Irving, A. J., McCallum, I. S. & Thirlwall, M. F. (1995). Strontium, neodymium, and lead isotopic evidence for the interaction of post-subduction asthenospheric potassic mafic magmas of the Highwood Mountains, Montana, USA, with ancient Wyoming craton lithospheric mantle. *Geochimica et Cosmochimica Acta* **59**, 4539–4556.
- Olafsson, M. & Eggler, D. H. (1983). Phase relations of amphibole-carbonate, and phlogopite-carbonate peridotite: petrologic constraints on the asthenosphere. *Earth and Planetary Science Letters* **64**, 305–315.

- Olson, P. (1988). Plume formation and lithosphere erosion: a comparison of laboratory and numerical experiments. *Journal of Geophysical Research* **93**, 15065–15084.
- Patchett, P. J., White, W. M., Feldmann, H., Kielinczuk, S. & Hofmann, A. W. (1984). Hafnium/rare earth element fractionation in the sedimentary system and crustal recycling into the Earth's mantle. *Earth and Planetary Science Letters* **69**, 365–378.
- Peate, D. W., Backer, J. A., Blichert-Toft, J., Hilton, D. R., Storey, M., Kent, A. J. R., Brooks, C. K., Hansen, H., Pedersen, A. K. & Duncan, R. A. (2003). The Prins of Wales Bjerge Formation lavas, East Greenland; the transition from tholeiitic to alkalic magmatism during Palaeogene continental break-up. *Journal of Petrology* **44**, 279–304.
- Puffer, J. H. (2001). Contrasting high field strength element contents of continental flood basalts from plume versus reactivated-arc sources. *Geology* **28**, 675–678.
- Ranganai, R. T., Kampunzu, A. B., Atekwana, E. A., Paya, B. K., King, J. G., Koosimile, D. I. & Stettler, E. H. (2002). Gravity evidence for a larger Limpopo Belt in Southern Africa and geodynamic implications. *Geophysical Journal International* **149**, 9–14.
- Riley, T. R., Leat, P. T., Storey, B. C., Parkinson, I. J. & Millar, I. L. (2003). Ultramafic lamprophyres of the Ferrar large igneous province: evidence for a HIMU mantle component. *Lithos* **66**, 63–76.
- Riley, T. R., Millar, I. L., Watkeys, M. K., Curtis, M. L., Leat, P. T., Klausen, M. B. & Fanning, C. M. (2004). U–Pb zircon (SHRIMP) ages for the Lebombo rhyolites, South Africa: refining the duration of Karoo volcanism. *Journal of the Geological Society, London* **161**, 547–550.
- Riley, T. R., Leat, P. T., Curtis, M. L., Millar, I. L., Duncan, R. A. & Fazel, A. (2005). Early–Middle Jurassic dolerite dykes from western Dronning Maud Land (Antarctica): identifying mantle sources in the Karoo large igneous province. *Journal of Petrology* **46**, 1489–1524.
- Riley, T. R., Curtis, M. L., Leat, P. T., Watkeys, M. K., Duncan, R. A., Millar, I. L. & Owens, W. H. (2006). Overlap of Karoo and Ferrar magma types in KwaZulu–Natal, South Africa. *Journal of Petrology* **47**, 541–566.
- Robinson, J. A. C. & Wood, B. J. (1998). The depth of the spinel to garnet transition at the peridotite solidus. *Earth and Planetary Science Letters* **164**, 277–284.
- Saunders, A. D., Storey, M., Kent, R. W. & Norry, M. J. (1992). Consequences of plume–lithosphere interactions. In: Alabaster, T., Storey, B. C. & Pankhurst, R. J. (eds) *Magmatism and the Causes of Continental Break-up*. Geological Society, London, Special Publications **68**, 41–60.
- Schärer, U. (1991). Rapid continental crust formation at 1.7 Ga from a reservoir with chondritic isotope signatures, eastern Labrador. *Earth and Planetary Science Letters* **102**, 110–133.
- Scherer, E., Münker, C. & Metzger, K. (2001). Calibration of the lutetium–hafnium clock. *Science* **293**, 683–687.
- Shaw, D. M. (1967). Trace element fractionation during anatexis. *Geochimica et Cosmochimica Acta* **34**, 237–234.
- Spera, F. J. & Bohron, W. A. (2001). Energy-constrained open-system magmatic processes I: General model and energy-constrained assimilation and fractional crystallization (EC-AFC) formulation. *Journal of Petrology* **41**, 999–1018.
- Sun, S. S. (1980). Lead isotopic study of young volcanic rocks from mid-ocean ridges, ocean islands and island arcs. *Philosophical Transactions of the Royal Society of London, Series A* **297**, 409–445.
- Sun, S. S. & McDonough, W. F. (1989). Chemical and isotopic systematics of oceanic basalts: implication for mantle composition and processes. In: Saunders, A. D. & Norry, M. J. (eds) *Magmatism in the Ocean Basins*. Geological Society, London, Special Publications **42**, 313–345.
- Sweeney, R. J. & Watkeys, M. K. (1990). A possible link between Mesozoic lithospheric architecture and Gondwana flood basalts. *Journal of African Earth Sciences* **10**, 707–716.
- Sweeney, R. J., Falloon, T. J., Green, D. H. & Tatsumi, Y. (1991). The mantle origins of Karoo picrites. *Earth and Planetary Science Letters* **107**, 256–271.
- Sweeney, R. J., Duncan, A. R. & Erlank, A. J. (1994). Geochemistry and petrogenesis of Central Lebombo basalts from the Karoo Igneous Province. *Journal of Petrology* **35**, 95–125.
- Taylor, S. R. & McLennan, S. M. (1995). The geochemical evolution of the continental crust. *Review of Geophysics* **33**, 241–265.
- Turner, S., Hawkesworth, C., Gallagher, K., Stewart, K., Peate, D. & Mantovani, M. (1996). Mantle plumes, flood basalts and thermal models for melt generation beneath continents: Assessment of a conductive heating model and application to the Parana. *Journal of Geophysical Research* **101**, 11 503–11 518, doi: 10.1029/96JB00430.
- Upton, B. G. J., Rämö, O. T., Heaman, L. M., Blichert-Toft, J., Kalsbeek, F., Barry, T. L. & Jepsen, H. F. (2005). The Mesoproterozoic Zig-Zag Dal basalts and associated intrusions of eastern North Greenland: mantle plume–lithosphere interaction. *Contributions to Mineralogy and Petrology* **149**, 40–56.
- Vervoort, J. D., Patchett, P. J., Blichert-Toft, J. & Albarède, F. (1999). Relationships between Lu–Hf and Sm–Nd isotopic systems in the global sedimentary system. *Earth and Planetary Science Letters* **168**, 79–99.
- Walter, M. J. (1998). Melting of garnet peridotite and the origin of komatiite and depleted lithosphere. *Journal of Petrology* **39**, 29–60.
- Watkeys, M. K. (2002). Development of the Lebombo rifted volcanic margin of southeast Africa. In: Menzies, M. A., Klempner, S. L., Ebinger, C. J. & Baker, J. (eds) *Volcanic Rifted Margin*. Geological Society of America, Special Papers **352**, 29–48.
- White, R. S. & McKenzie, D. P. (1989). Magmatism at rift zones: the generation of volcanic continental margins and flood basalts. *Journal of Geophysical Research* **94**, 7685–7729.
- White, R. S. & McKenzie, D. (1995). Mantle plumes and flood basalts. *Journal of Geophysical Research* **100**, 17543–17585.
- Wigley, R. (1995). The geochemistry of the Karoo igneous volcanic and intrusive rocks of Botswana, PhD thesis, University of Cape Town, 182 pp.
- Woodhead, J. D., Hergt, J. M., Davidson, J. P. & Eggins, S. M. (2001). Hafnium isotope evidence for ‘conservative’ element mobility during subduction zone processes. *Earth and Planetary Science Letters* **192**, 331–346.
- Zhang, X., Luttinen, A. V., Elliot, D. H., Larsson, K. & Foland, K. A. (2003). Early stages of Gondwana breakup: the $^{40}\text{Ar}/^{39}\text{Ar}$ geochronology of Jurassic basaltic rocks from western Dronning Maud Land, Antarctica, and implications for the timing of magmatic and hydrothermal events. *Journal of Geophysical Research* **108**, 2249.
- Zindler, A. & Hart, S. (1986). Chemical geodynamics. *Annual Review of Earth and Planetary Sciences* **14**, 493–571.